INTEGRATION OF OPTICAL STRUCTURES WITH CHIRAL NANOCELLULOSE FILMS

A Dissertation
Presented to
The Academic Faculty

by

Shengtao Yu

In Partial Fulfillment
of the Requirements for the Degree
Master in the
Materials Science and Engineering

Georgia Institute of Technology
August 2019

INTEGRATION OF OPTICAL STRUCTURES WITH CHIRAL NANOCELLULOSE FILMS

Approved by:

Dr. Vladimir V. Tsukruk, Advisor
School of Mateirals Science and Engineering
Georgia Institute of Technology

Dr. Zhiqun Lin
School of Mateirals Science and Engineering
Georgia Institute of Technology

Dr. Wenshan Cai
School of Electrical and Computer Engineering
Georgia Institute of Technology

Date Approved: April 30, 2019

ACKNOWLEDGEMENTS

I would like to express sincere gratitude to my advisor, Dr. Vladimir V. Tsukruk, for his constant support and guidance. He provided me with the precious research opportunity and freedom for exploration and helped me identified my research topic with insightful advice. Without his support, this research work would never have happened, I would never have grown up with profound knowledge and useful techniques in this research field.

I would like to thank current and previous colleagues in SEMA lab at Georgia Tech. Special gratitude goes to Dr. Chun-Hao Lin, who introduced me to the project, trained me on various experimental methods, and also gave me many useful suggestions on my research. I also would like to acknowledge contribution from Dr. Rui Xiong, he helped me improve my experiments design, data organization and writing skills. Over the past three years, I have been helped by many colleagues on both research and life. I would like to thank current SEMA lab members, including Marcus Smith, Anise Grant, Andrew Erwin, Jing Zhou, Shuaidi Zhang, Michelle Krecker, Katarina Adstedt, Hansol Lee, Dr. Saewon Kang, and Dr. Minkyu Kim. I also would like to thank previous members, including Dr. Sidney Malak, Dr. Ren Geyark, Dr. Cherpak Vladyslav and Dr. Ruilong Ma. Without their professional and warm-hearted support, I would never have achieved such progress in my work.

I also would like to acknowledge contributions from collaborators, especially members from Dr. Zhiqun Lin's lab, including Dr. Young Jun Yong, Gill Biesold-Mcgee, Yajing Chang. They have enabled my research works with great materials support.

Support for this project also came from Institute of Electronic and Nanotechnology of Georgia Tech, especially from Devin Brown, Charlie Turgeon, Eric Woods, and Tran-Vinh Nguyen.

Lastly, I would like to thank my family, even we are physically separated by an ocean, their understanding and encouragement from home has supported me all the time through the graduate program.

TABLE OF CONTENTS

LIST OF TABLES

LIST OF FIGURES

LIST OF SYMBOLS AND ABBREVIATIONS

AFM	Atomic Force Microscope
CD	Circular Dichroism
CNC	Cellulose Nanocrystal
CNF	Cellulose Nanofiber
CP	Circular Polarization
DI	Deionization
EISA	Evaporation-Induced Self-Assembly
FCC	Face-Centered Cubic
FWHM	Full Width at Half Maximum
HPC	Hydroxypropyl Cellulose
ICP	Inductive Coupled
IPA	Isopropanol alcohol
nIR	near-Infrared
LC	Liquid Crystal
LCP	Left-handed Circular Polarization
NA	Numerical Aperture
PDMS	Poly(dimethylsiloxane)
PEG	Poly(ethylene glycol)
PEI	Poly(ethyleneimine)
PMMA	Poly(methyl methacrylate)
POM	Polarized Optical Microscope
PS	Polystyrene

PVA	Poly(vinyl alcohol)
QD	Quantum Dot
RCP	Right-handed Circular Polarization
RGB	Red-Green-Blue
RIE	Reactive Ion Etching
SEM	Scanning Electron Microscope
TPIP	Two-Photon Induced Polymerization
UV	Ultra-violet
λ	Wavelength
θ	Angle
D, d	Periodicity in distnace
f	Focal Length Pitch distance
I	Light intensity
m	Mode number of diffraction
n	Refractive Index
P, p	Pitch distance of chiral stacking
R	Surface curvature of lens

SUMMARY

Generation of circularly polarized (CP) light *via* cellulose nanocrystals (CNC) has demonstrated great potential for next generation of chiroptical materials, thanks to the abundance, cost-effective preparation, as well as the retained chiral liquid crystal ordering in solid form. To enhance the chiroptical properties of CNC film, a convenient strategy capable of integrating both diffractive and refractive optical structures is developed based on top-down lithographic techniques and bottom-up evaporation-induced self-assembly. The feasibility of such strategy is proved by a few optical structures including photonic gratings, photonic crystals and micro-lenses. The successful integration of these extrinsic structures with intrinsic chiral structure of CNC is evidenced by preservation of helical stacking structure of CNC as well as a good registration of features size down to sub-micron level with uniformity across large area on the film surface. As a result, a combination of more accurate and sharper structural color, light focusing capability as well as enhanced circular dichroism is observed, indicating great potential in advanced optical systems based-on CP light. This is the first study to manipulate and enhance the chiroptical properties of CNC with artificial photonic structures, while the unconventional hybrid strategy demonstrates a fledgling, yet promising method for development of hierarchical biophotonic materials in general.

CHAPTER 1. INTRODUCTION

Light is essential for most livings beings on earth.[1] The capability to detect, harvest, or even responsively react to light has been optimized by evolution over millions of years.[2], [3] As a result, nature has produced a huge library of micro-/nano-structures with wide range of photonic and optical functionalities,[4] including vivid iridescence, anti-reflection, chiral polarization, and intensity enhancement.[5], [6], [7] More and more advanced optical materials have been designed based on inspiration from naturally occurring optical structures.[8], [9] The trend is revealed in publication activity, as shown in Figure 1.

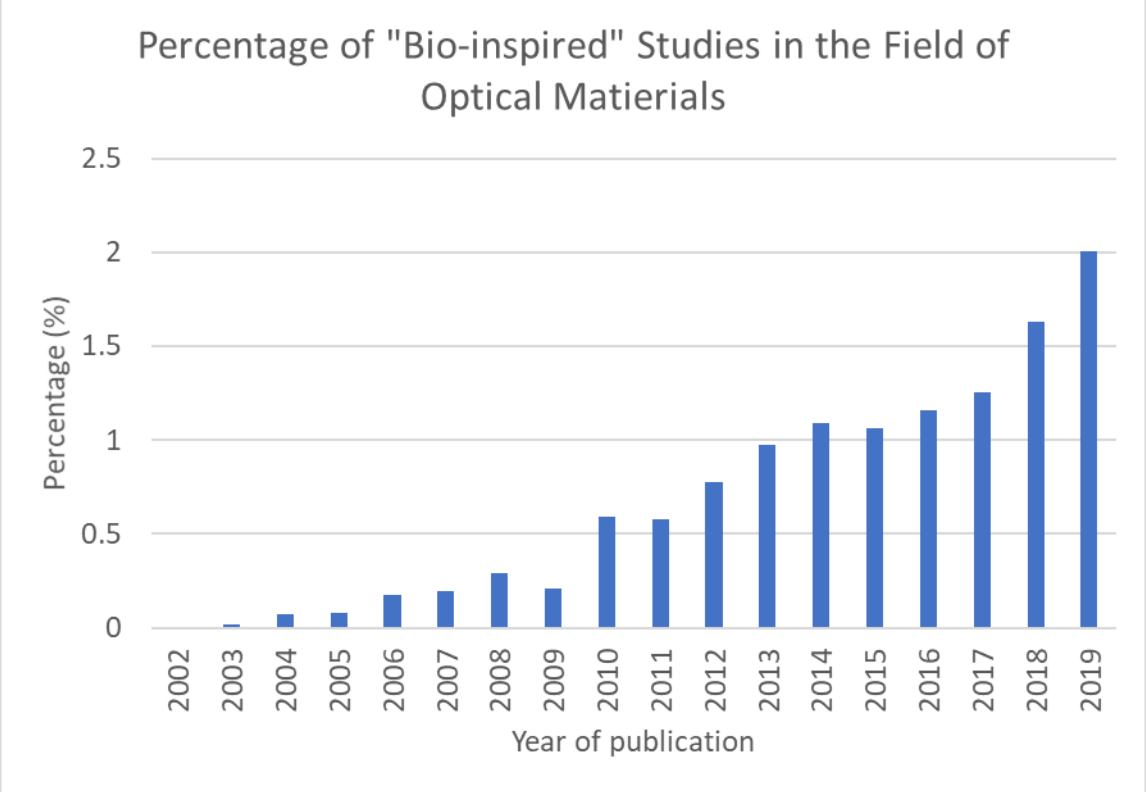

Figure 1 Percentage of bio-inspired researches in the field of optical materials. Data is obtained from Scopus of Elsevier B.V.

1.1 Photonic structures in nature

Among various exquisite photonic/optical structures found in nature, one dimensional (1D) diffraction gratings/multi-layers, chiral phase and micro-lenses are three representative structures with ordering and geometry in different dimensions and length scales.[10]

1.1.1 Diffractive structures in nature

Light interference from periodic diffractive structure is widely found in nature, especially in iridescence of shells of mollusks, wings or exoskeleton of insects and leaves, petals and fruits of plants.[11], [12], [13] The light diffraction-based optical responses are generated by surface gratings or multi-layered structures.

The diffraction gratings can interact with incident light to modulate its phase and/or amplitude. For ideal gratings as shown in Figure 2a,[14] the diffraction equation governing the primary wavelength constructively interfered, λ_g is:

$$m\lambda_g = D \cdot (sin\theta_I + sin\theta_D) \quad (1)$$

Where m is the order of diffraction mode, D is the periodicity of the grating, and θ_I , θ_D are incident angle and observation angle, with respect to substrate normal, respectively.[14]

Based on this equation, the observed coloration is determined by the grating spacing and viewing-angle. In the plane perpendicular to the direction of the gratings, incident white light will be dispersed into rainbow-like pattern. As for the observer, the structure

color will redshift via increasing grating spacing or tilting viewing position from vertical to glancing angle.

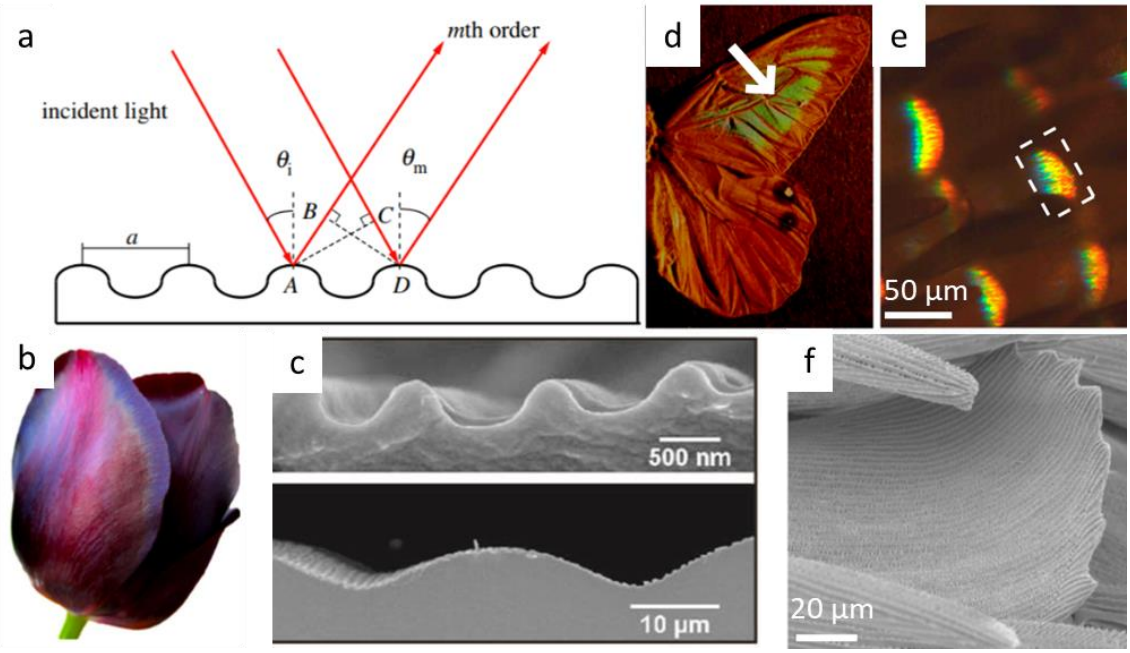

Figure 2 Light diffraction on surface gratings structures and examples in nature. Figures are obtained from [14-17].

Example of such grating structure is widely found in flowers of plants.[14], [15] For instance, petals of *Hibiscus trionum*, *Tulipa Kaufmanniana and Tulipa kolpakowskiana* display gorgeous metallic coloration (Figure 2b),[15], [16] which are generated by the diffraction from surface striation or ridges (Figure 2c). Such periodic structures are formed on the waxy cuticle layer on the epidermal cells, possibly induced by buckling of cuticles during the isotropic growth of petal.[17] At closer examination at the grating structures, the epidermis is characterized separately, and diffraction signal in visible range is found to be broader in angle distribution, comparing to ideal gratings, this is explained by the curvature and presence of natural disorder.[14]

Variation of grating structures are found in butterfly wings. One example is found from the fore- and hind wings of *P. luna* males (Figure 2d).[11] In contrast to conventional gratings, its angle-dependency of coloration is reversed, and can be described by the following equation 2:

$$m\lambda_g = D \cdot (\cos\theta_I + \cos\theta_D) \quad (2)$$

Where physical meaning of *m*, λ_g, D, θ_I and θ_D all remain the same as in equation 1, while the geometric relation change from $sin\theta$ to $cos\theta$. This anomalous diffraction is due to the change of direction of the gratings. Instead of paralleling to surface, this grating is vertical to the surface of the scales. The tissue with normal gratings is termed "scallop", as narrow stripes on top of curved plates on scales, as shown in Figure 2e.

Similar to grating structures, multilayers-structure produce interference with highly-ordered periodic structures in one dimension, while the orientation with alternating refractive is vertical to the surface. As demonstrated in Figure 3a, layers of two materials with different refractive indices are arranged periodically, where the light travels through with different incident angles, and is reflected at every interfaces, resulting in interference.[14] Such multilayer structure acts as a color filter, increases transmitted light with certain wavelength range and strengthens reflect light with complementary color.

Two mathematical relationships need to be met for strongest constructive interference at a selected wavelength. First, phase difference through a double layer is integer times of the wavelength, which can be described as in equation 3:

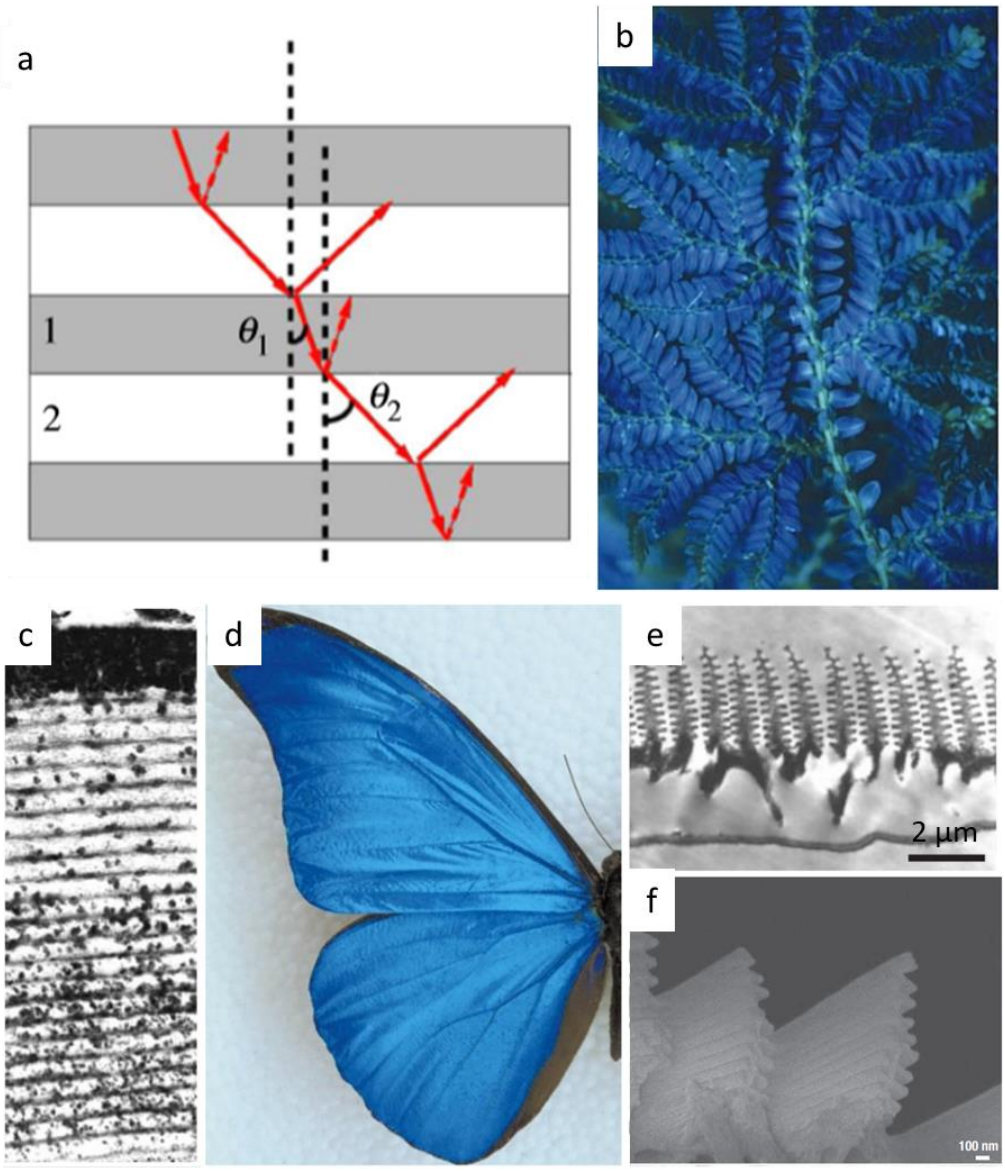

Figure 3 Light diffraction by multilayer structures and examples in nature. Figures are obtained from [10], [14], and [19].

$$m\lambda_g = D \cdot (\cos\theta_I + \cos\theta_D) \tag{3}$$

Where the physical meaning of m, λ are the same, while n_1 and n_2 are the refractive indices of the double layer ($n_1 > n_2$); d_1, d_2 are their thickness and θ_1, θ_2 are incident

angles (Figure 3a), respectively. Second, interference between light from neighboring layer 1 and 2 are deconstructive, which can be described as equation 4:

$$\left(m' - \frac{1}{2}\right)\lambda = 2n_1 d_1 \cos\theta_1 \quad (4)$$

Where $m' \leq m$. For selective color reflection/transmittance obtained with multilayers with less regularity, transfer matrix approach can be utilized to calculate the optical response.[18]

Such multilayer structure widely found in species including epidermal cell walls of young leaves of *Selaginella*, iridescent ferns like *Danaea nodosa and Lindsaea lucida*, and protoplast in leaves of *Begonia pavonina* and *Trichomanes elegans*, and "iridosome" structure in fruit of *Elaeocarpus angustifolius*. Specifically, Figure 3b shows the blue structural color from young leaves of *Selagniella*, which is reported to be a mechanism to protect the leaves against Ultraviolet (UV) light with the constructive interference in reflection mode. A typical cross-section of such multilayer structure (*Diplazium tomentosum*) is shown in Figure 3c,[10] where alternating layers formed by fibers of cellulose can be observed.

Another good example of biological multilayer interference is the iridescence from Blue *Morpho rhetenor* butterfly, which is vivid blue (Figure 3d) and can be observable from very long distance.[19] In this case, the two materials are cuticle (n_1=1.56) and air (n_2=1) on the scale, while the thickness of a double layer ($d_1 + d_2$) is about 200 nm. The discrete layering is shown as cross-sections in Figure 3e and 3f.[19] In addition, the tilt of

the multilayer structure at about 15° is found to increase the broad angle of reflected intensity.

1.1.2 Chiroptical structures in nature

As an important variant the multilayer optical structure, helicoidal layering (called twisted plywood or helicoidal Bouligand structure) are also found in nature, which generate circular polarization and vivid iridescence at the same time.[20] Such additional optical response with strong circular dichroism is not derived from chirality in molecular level, but in a higher scale with the helical arrangement of repeating unit analogous to cholesteric liquid crystalline structure.[10], [21] In such structure, chitin microfibril or cellulose nanocrystal is the repeating unit, which possesses high aspect ratio and aligns to one director in one layer, while the orientation of director gradually twists across neighboring layers until 360° to form a pitch.[22] The helical arrangement is drawn in Figure 4a, where

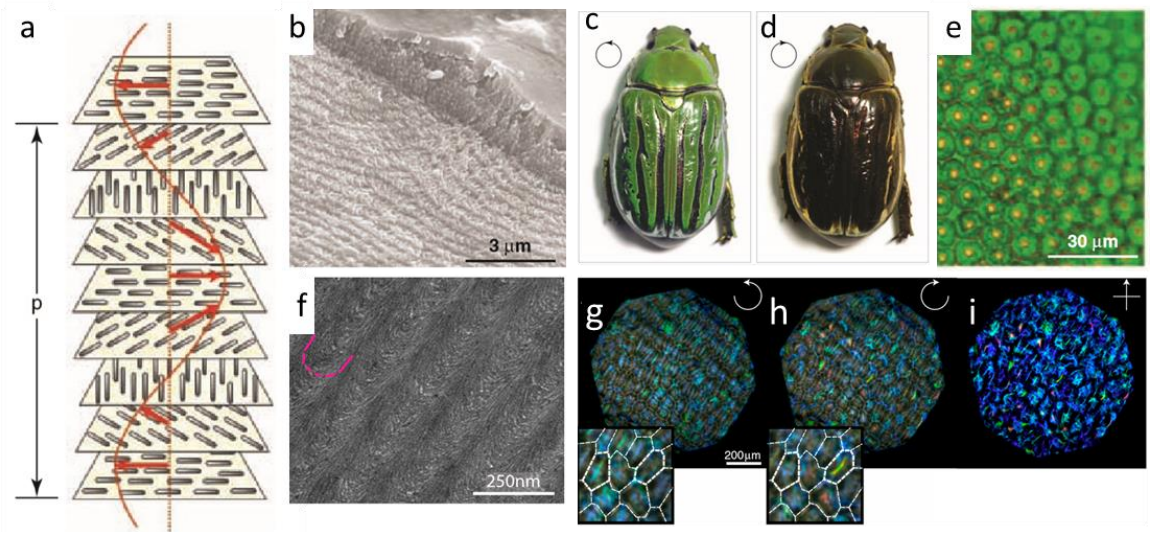

Figure 4 Chiral nematic structures and examples in nature. Figures are obtained from [22], [23].

a left-handed helix of pitch *p* is sketched, the orientation of director (red arrow) traces the helix while advancing through layers.

Because of such chiral structure, incident light with the same handedness of circular polarization is selectively reflected, while only light with the opposite handedness is transmitted. Besides the polarization, the spectra selectivity can be described by equation 5[22]:

$$m\lambda = n \cdot p \cdot \cos\theta \tag{5}$$

Where m is the mode number of interference, λ is the maximum wavelength under constructive interference, n is the average refractive index, p is the pitch distance while θ is the incident and reflection angle (assume to be the same).

Specific examples could be found in exoskeletons of beetles, shrimps and crabs, leaves and fruits of plants.[23] For instance, as shown in Figure 4b, the cross-section of the exoskeleton *Chrysina gloriosa* shows layering structure of helical order under the waxy layer. Thanks to such long-range ordering of chitin fibrils, the beetle shows green structural color only under left-handed polarizer but appears to be dark under the right-handed one, the stark contrast is shown in Figure 4c and d. Interestingly, the helicoidal structures arrange into pentagon- and hexagon-shaped domains (~10 μm) with hexagonal packing (Figure 4e), as an efficient way to fill the surface of exoskeleton while accommodating the natural curvature. Such microdomains are found to be focal conic domains, demonstrating two reflection maximum at 530 nm and 580 nm and broad spectra.

Different from single-handedness as discussed in the beetle exoskeleton, coexistence of right- and left-handed polarization is observed in structural color. For instance, fruit of *Pollia condensata* shows iridescence with polarization in both handedness. [22] The left-handed helical stacking (highlighted by red lines) is identified in the thick cell wall layer of the fruit (Figure 4f). As a result of helical stacking, vivid iridescence is observed under cross-polarizer (Figure 4g) and it has strong component in both left- (Figure 4e) and right-handed (Figure 4f) circular polarization. Because no right-handed helical structure has been directly observed, the mechanism of both chirality in reflection is not fully understood. However, it is assumed that the chirality of stack of cellulose microfibrils is independent of chirality of the individual microfibril. [22] Besides, the twisting direction of the microtubule during cell growth is either clockwise and anticlockwise, which could possibly induce the right-handed helical stacking and corresponding right-handed polarized structure color. [24] Another example of coexistence of both handedness is found in beetle *Plusiotis resplendens*. The beetle's exocuticle layer is composed of a sandwiched structure with two left-handed helical layers on the two sides and a middle layer with vertical aligned chitins. As a result, left-handed polarized light is generated with one layer of helical structure, while the right one is produced by reflection from lower layer and sign-reversion of handedness through the middle layer, which function as a half-wave plate. [25]

1.1.3 Micro-lens structures in nature

In addition to the diffraction-based photonic structures of gratings and multilayers, where spectra and polarization of light is modulated, optical structures that control the propagation directionality of the light based on refractive behaviour are also widely found

in nature.[26] One good example is the micro-lens structure, typically exist in the form of array. Micro-lens arrays with different geometries, symmetry and periodicities are observed from eyes of insects, skin of marine species, and surface layer of petals and leaves plants.[27]

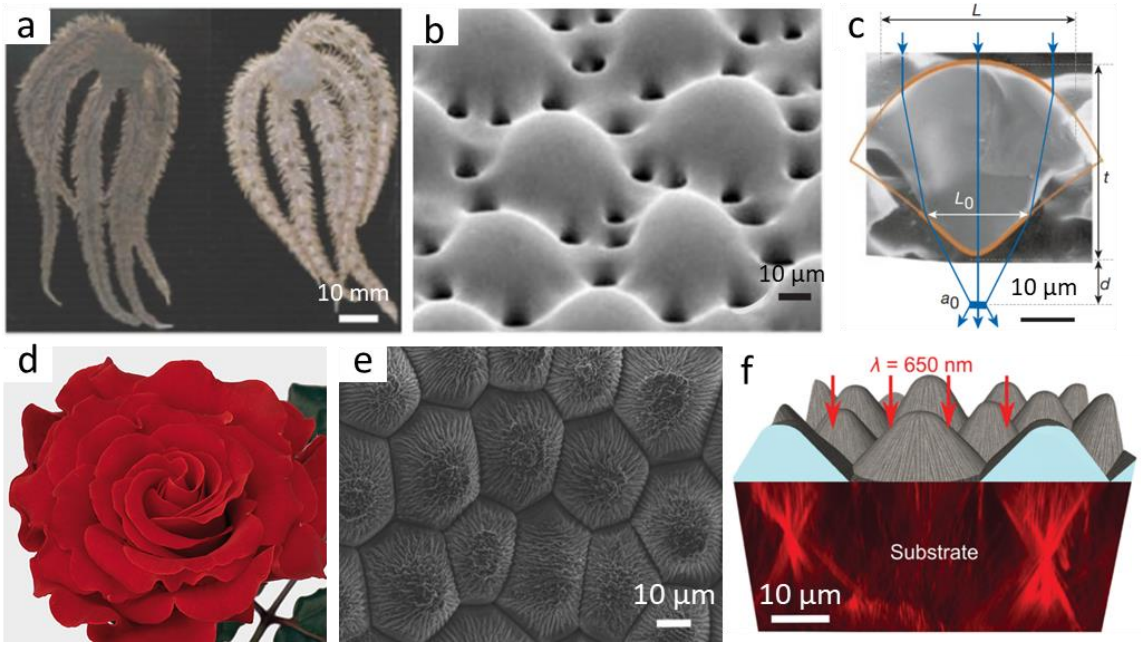

Figure 5 Micro-lens structures in nature. Figures are obtained from [28], [29].

On one hand, for individual micro-lens or lens in general, light focusing capability is determined by several parameters of the lens, both geometrical and material-related, including the curvature, thickness, and refractive indices of the lens. By knowing these parameters, along with the environment refractive index, focal length can be determined with equation 6.[28]

$$f = \left(\left(\frac{n_L - n_0}{R_1}\right) + \left(\frac{n_0 - n_2}{R_2}\right) - \left(\frac{n_L - n_0}{R_1}\right)\left(\frac{n_0 - n_L}{R_2}\right)\left(\frac{t}{n_L}\right)\right)^{-1} \quad (6)$$

Where f is the effective focal length; R_1 and R_2 are curvatures of the front surface and rear surface, respectively; n_L and n_0 are refractive indices of the lens and space (air), respectively; t is the center thickness of the lens. For planer lens, $R_1 = +\infty$, or $R_2 = -\infty$. On the other hand, the array ordering is responsible to accommodate the surface of tissues or organs in terms of their larger curvatures, and to collect light from a wider angle in some applications. [7], [29]

A good example of such optical structure is the array of double-lens design found in the Brittlestar *Ophiocoma pumila* and *Ophiocoma wendtii*.[7] These brittlestars are light-sensitive, as shown in Figure 5a, the *O. wendtii* shows different appearance under different illumination, it appears to be dark brown during the day and changes to banded grey and black at night. Such sensitivity to light is due to the three-dimensional mesh of skeletal structure locate on every joint of arms.

To be specific, the micro-lenses in *O. wendtii* are enlarged spheres of the calcitic exoskeleton, with typical diameter from 40 to 50 μm. As shown in Figure 5b, is a zoom-in image of the micro-lenses while the cross-section of the double-lens design is shown in Figure 5c. These micro-lens are found to be quite regular, and the optical axis of the calcite is found to be parallel to the lens axis (marked) and perpendicular to the surface of the exoskeleton mesh.[29] With the help of these micro-lens to enhance the incoming light intensity on photoreceptors, it is reported that the brittlestar can escape from predators by detecting the shadow, even without any specialized organ like eyes.[29]

Micro-lenses are also widely present in plants to sustain the photosynthesis at low light environment (leaves) or to enhance the color saturation (petals). Like the anti-

reflection micro-cones found in moth eyes, “micropapillaes” are present on petals of roses *Rosa El Toro* (Figure 5d). A typical micropapilae has an average width at 32 μm and height at 19 μm, as shown in Figure 5e. Besides antireflection functionality, the structure yield a higher light collection due to broadband and omnidirectional optical transmittance. It is also reported that this morphology could increase the optical path, due to redistribution of light beneath. Such mechanism is sketched in Figure 5f.[28]

1.2 Fabrication approaches of photonic structures

1.2.1 Bottom-up approaches

Utilizing the interaction among building blocks at scales ranging from molecular to colloidal microparticle level, bottom-up assembly methods are developed to form photonic/optical materials with well controlled periodicity and symmetry. Such bottom-up approaches, including both layer-by-layer deposition for multilayers and self-assembly of colloidal particles for photonic crystals, are advantageous for hierarchical structures across length-scales. However, they are sensitive to processing conditions including pH, temperature and humidity, which will influence the organization of the final architecture.[30]

First, multilayer structures as discussed in part 1.1.1 can be constructed with layer-by-layer method. The refractive index contrast needed for such one-dimensional photonic crystal is achieved by pairing of materials chosen from one or both categories of inorganic and organic materials. Several techniques are used for layer deposition, including spin-coating, dip-coating, Langmuir-Blodgett coating and spray coating, based on the precursors physical status and chemical properties. As a classic example, uniform layers

of TiO2 (n=1.74) and SiO2 (n=1.22) are deposited alternatingly. By controlling the specific thickness, porosity, and surface topography, the refractive index contrast can be increased to about 0.85.[31] As a result, reflection in visible range of such a stack of a few

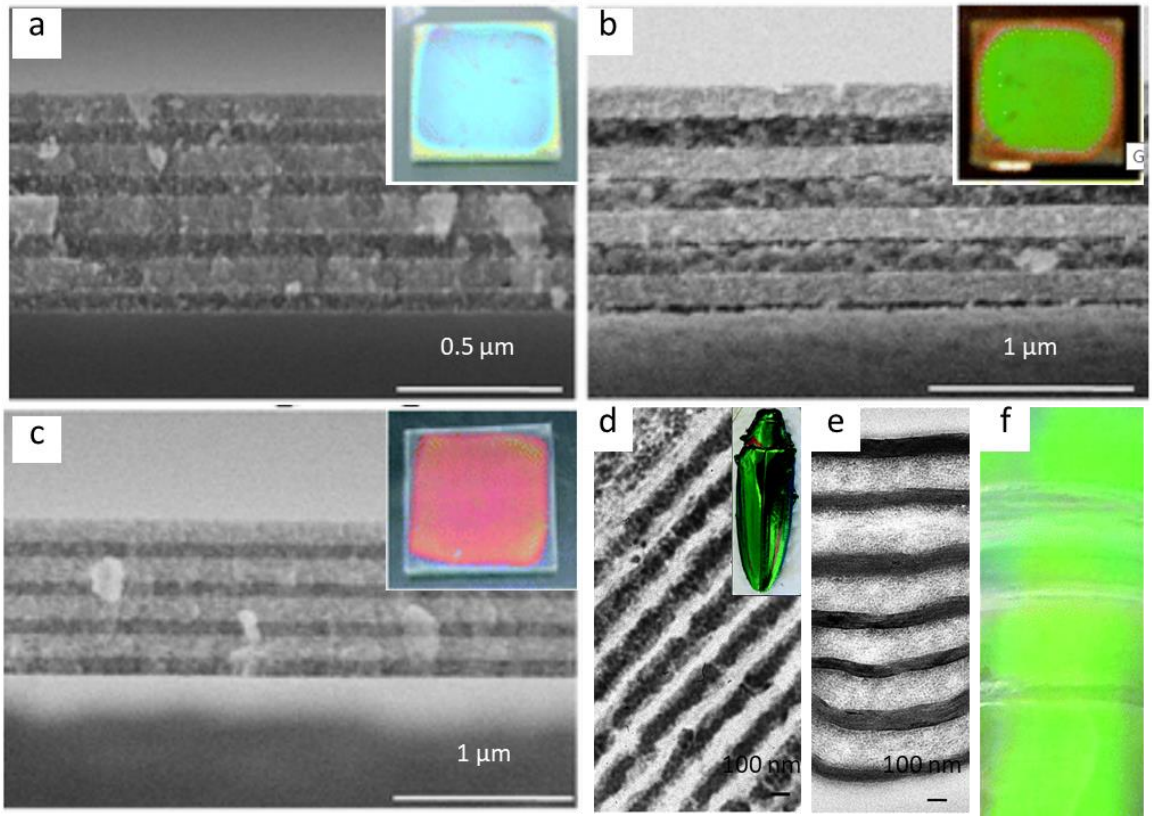

Figure 6 Multilayer structures fabricated through Layer-by-Layer deposition. Figures are obtained from [32], [35].

double-layers can reach around 65% by interference, demonstrating vivid structure color. [32], [33] The tunability over the photonic band gap is demonstrated in Figure 6 a-c, by choice of the oxides in bi-layers, blue (SiO2/TiO2), green (SiO2/SnO2), and red (SnO2/TiO2) iridescent in reflection under natural light can be observed.[32]

Same strategy can be applied on biopolymers easily. For instance, with the spin-assisted LbL assembly of Titanate/silk (n=1.82) and silk (n=1.56), vivid iridescence is observed at the peak at 385 nm.[31] And cellulose nanofibrils with poly(vinyl amine) are

also reported to form LbL photonic films.[34] Another example of such bilayer structure is shown in Figure 6f, learning from the multilayer structure of the green iridescent eletron of *Chrysochroa rajah* beetle (Figure 6d), layers of poly(ethylenimine) (PEI)/vermiculite clay with high refractive index is paired with SiO2/CNC layers. As a result, the stack thickness is fine-tuned (Figure 6e) to mimic the vivid green structural color, as shown in Figure 6f.[35]

Assembly of colloidal nanorods into layers is also a good example of bottom-up approach to fabricate photonic structures.[30], [36] One of the most popular one is cellulose nanocrystal, the evaporation induced self-assembly of which is well investigated for the unique photonic properties with chirality.[37] More detailed discussion on mechanism and control of chiral ordering can be found in part 1.3.

More importantly, assembly of colloidal microspheres is more versatile and efficient to construct photonic crystals with periodicity from 1D to 3D.[36] Microspheres made of polystyrene (PS) and SiO2 are the most popular building blocks due to their good uniformity of shape and size, and availability.[38], [39] Driven by capillary force, the colloidal building blocks assemble into close-packed structure of face-centered cubic (FCC) structures, also known as "opal" structures, with well-defined photonic band gap due to good uniformity.[40] Besides, the inverse opal structure can be obtained by using the assembled structure as template for a secondary materials, and subsequent removal of the assembled structure by solvent dissolution or thermal decomposition.[36]

In addition, such colloidal assembly could be realized on binary building-blocks as well.[41] As shown in Figure 7a, 2D photonic crystals are assembled using Langmuir trough.

To be specific, colloidal beads with diameters at 1063 nm and 225 nm were first compressed and assembled on water-air interface, subsequent lowering of the interface assists the transfer of close-packed monolayer onto the silicon wafer. After water is dried, distinguish coloration can be observed at the surface, indicating successful assembly of 2D

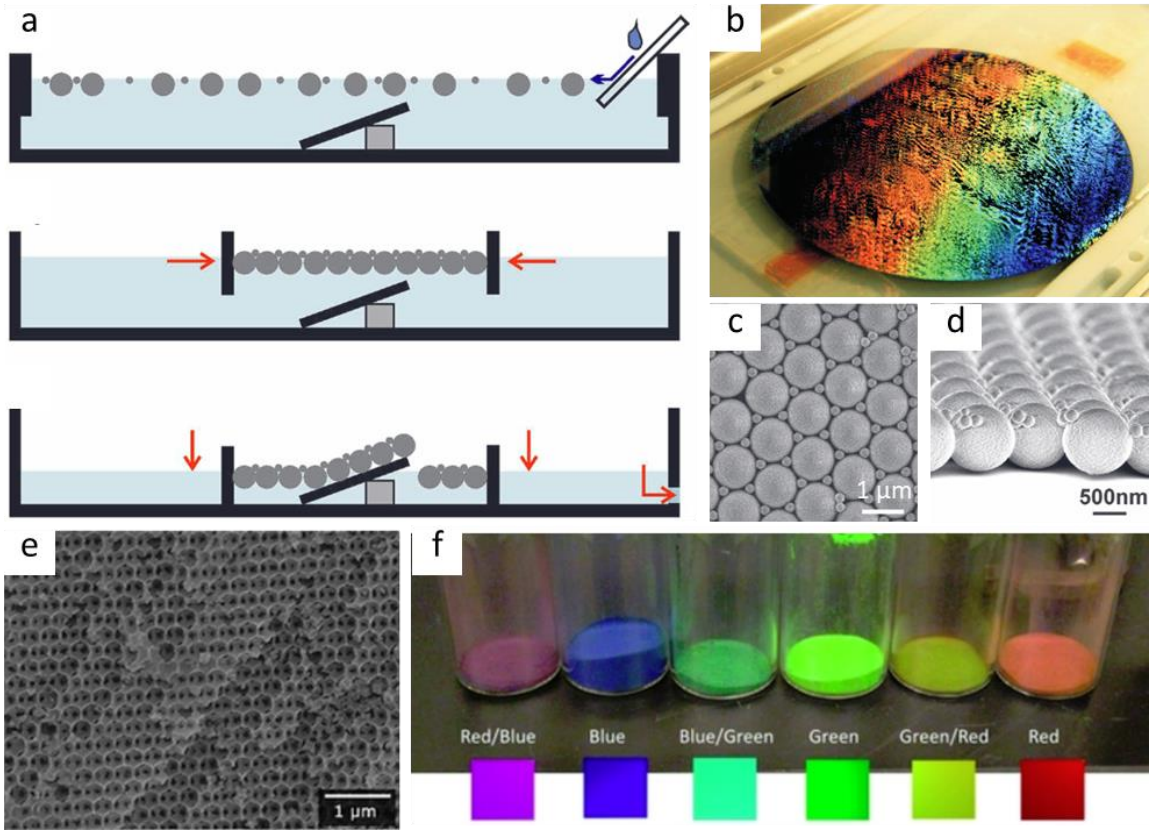

Figure 7 Colloidal microspheres assembly for photonic structures. Figures are obtained from [41], [43].

photonic crystals (Figure 7b). The assembled structure also demonstrated good uniformity with small particles filling interstitial sites regularly (Figure7c). In this study, researchers also demonstrated controllable varieties of binary assembly by stoichiometry (Figure 7c, d).[41]

As for inverse opal photonic structures, a wide range of secondary materials have been utilized, including oxides (Al2O3, TiO2), quantum dots (CdTe, CdS) and biopolymers (silk fibroin, nanocellulose).[42] For instance, thee-dimensional ordered macroporous (3DOM) SiO2 structure were obtained by pyrolysis method to remove assembled opal structure of poly(methyl methacrylate) (PMMA).[43] A typical inverse opal structure of the SiO2 is shown in Figure 7e, where long range order is retained in three-dimension. Interestingly, it is demonstrated that the resulting powder of 3DOM SiO2 maintains vivid structural color, which is adjustable by the pyrolysis temperature, even with same size of the PMMA particles. The wide spectra obtained by this method is demonstrated in Figure 7f. One great advantage for this material for pigment is the additive coloration, unlike the conventional subtractive color by absorption of dyes.[43]

1.2.2 Top-down approaches

As the photonic structures requires periodic distribution of materials in forms of layers, ridges, particles or more complex architectures with precisely controlled shapes and locations, especially for coherent light scattering where precise phase differences is produced when light interact with the corresponding micro-/nano-structures.[13] Thanks to the development of micro-fabrication techniques especially driven by the innovations from the semiconductor industry, several lithographic, printing, and laser interference techniques have been created and improved to achieve features such as high-resolution, large-area and even three-dimensional capability for patterning of photonic structures or creating of optical structures at micro-scale.[44]

First of all, lithography strategies based on radiance of light, including UV light, visible continuous-wave laser, near infrared (n-IR) femto-second laser, X-ray, and electron beam are all explored to date. A common feature shared by these lithographic methods is use of photomasks, or computer assisted focused beam of laser or electron to transfer contrast of exposure dosage to physical patterns.[45]

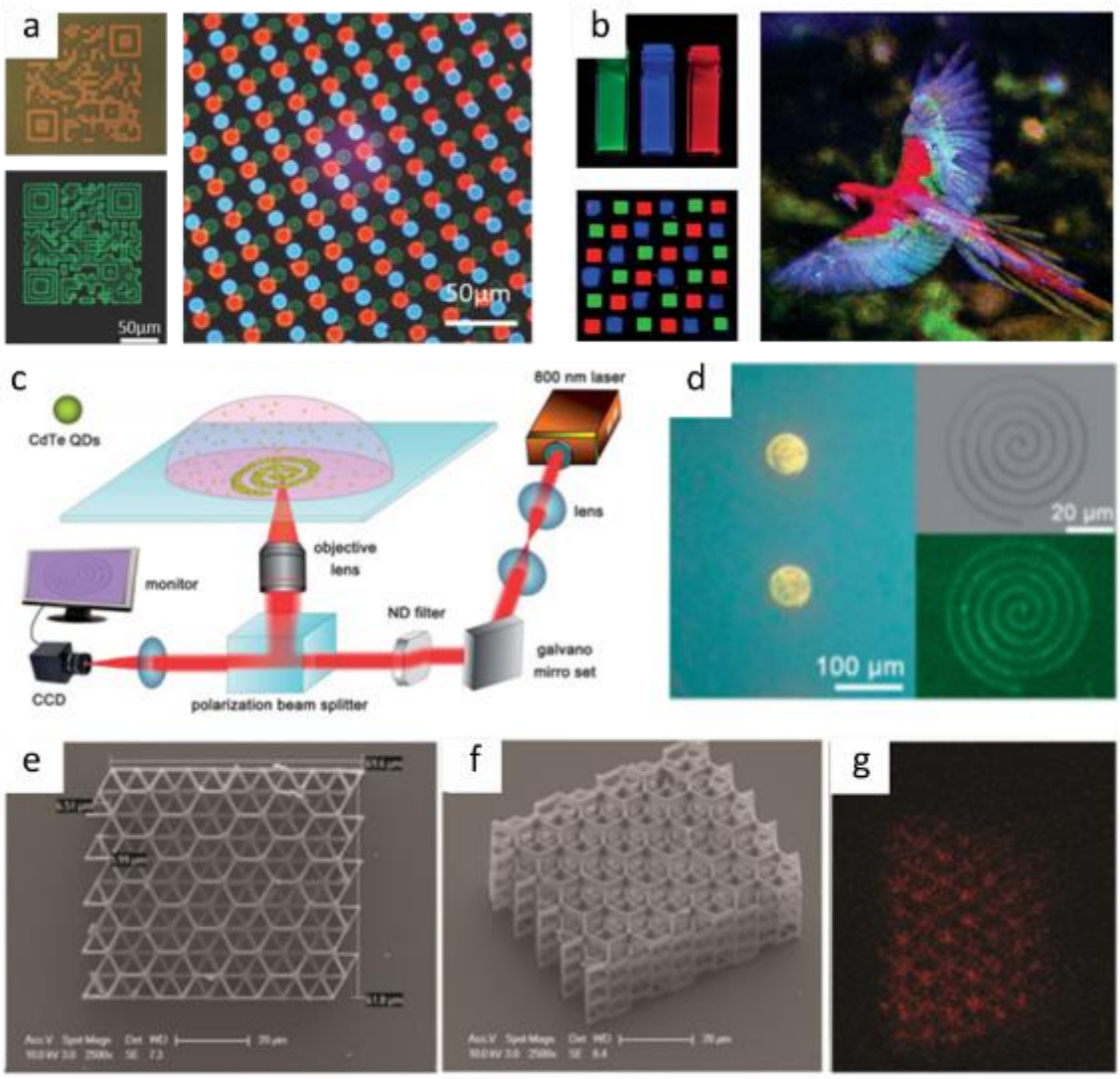

Figure 8 Lithographic methods for advanced photonic/optical structures. Figures are obtained from [48-52].

State-of-the-art of photonic structures fabricated by photolithography is exemplified by patterning of Cd-based colloidal quantum dots (with functionalized ligands as cross-linker)[46] and perovskite quantum dots (with orthogonal photoresist)[47], as shown in Figure 8a). Notably, the latter photolithography process has successfully fabricated various patterns including Red-Green-Blue (RGB) pixelated pattern, as well as high resolution lasing cavity with quality factor at 500~600. More recent development of

lithography approaches simplifies the process. For instance, direct photolithography via photoresist-free approaches has also been reported.[48] Researchers utilized solubility change of several photosensitive inorganic ligands that binds to surface of quantum dots. In one case, CdSe quantum dots were capped with ammonium 1,2,3,4-thiatriazole-5-thiolate ($NH_4CS_2N_3$), which provided good colloidal stability in dimethylformamide (DMF) and dimethylsulfoxide (DMSO). Upon UV irradiation at 254 nm for a dosage about 120 mJ/cm^2, the $NH_4CS_2N_3$ ligands decomposed and became insoluble. The unexposed quantum dot solution was then washed off. With the help of a mask, photopatterning at comparable resolution with conventional photolithography was made possible, the multicolor patterning capability is shown in the Figure 8b.[48]

To better fabricate arbitrary pattern without the constraint from rigid and expensive photo masks, laser direct writing was introduced. With the help of near-IR femto-second laser, this technique utilized optical gradient force generated by the focused laser beam, which drives the assembly of nanoparticles in water solution towards sites on the laser scanning track (Figure 8c).[49] It is worth noting that, the usage of femtosecond laser is crucial for effective thermal relaxation to avoid bulky aggregation of the nanoparticle, which is an important standard for laser direct writing guided assembly. The highest resolution reported is about 170 nm. Arbitrary micropatterns fabricated is also shown in Figure 8d.[50]

Extending patterning from 2D to 3D, technique using nIR femtosecond laser has also been developed via two-photon initiated polymerization (TPIP) of polymer-nanoparticles composites. In particular, Dr. Kwang-sup Lee's group have optimized this method with years of research work.[51], [52] In principle, a critical issue is to effectively

disperse nanoparticles with the polymeric matrix with high enough loading. In this development, functionalized nanoparticles can be chemically bonded to the resist for TPIP. The capability of this technique to fabricate arbitrary 3D nanostructure is also demonstrated in Figure 8e-g). Other photonic structures, including noble metal coated micro-helix for meta-materials and 2.5D geometries for diffractive optical properties are also demonstrated based on the TPIP.[53], [54]

Nanoimprint lithography, or hot embossing, is a molding technique, where hard mold with predefined nano- or micro-structure is tightly pressed on "thermal resist" layer of polymer like polydimethylsiloxane (PDMS) on flat hard substrate, while the system is heated above the glass-transition temperature of the resist polymer.[55] In some cases, UV light curing can also be used to assist the molding.[56] After the fluidic polymer filled receding part of the mold by capillary force, the system is then cooled down to room temperature and the mold is released from high pressure. The unwanted residue resist, can be removed by a dry etching process, exposing the underlying substrate, which enables a second etching process if pattern into the hard substrate is needed. Unlike lithography methods using UV-light, or laser, nanoimprint is not limited by diffraction of light, and can be done in a fast and convenient manner. In addition, the parallel nature, along with the compatibility for roll-to-roll process, make this technique a promising large scale, low-cost fabrication with precision at the level of sub-10 nm. The resolution, however, is highly dependent on the mold, which is typically made by electron-beam lithography.[57]

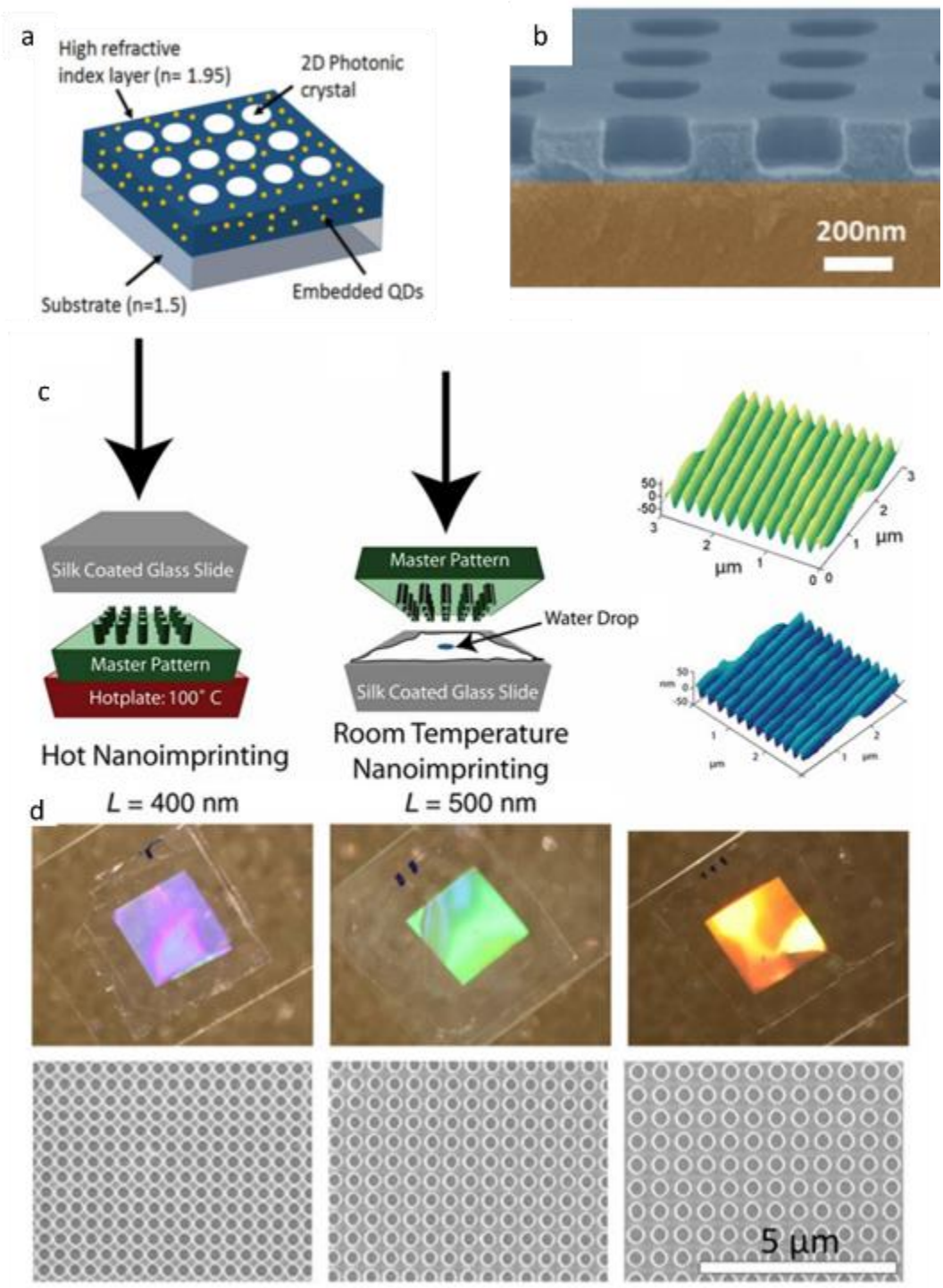

Figure 9 Nanoimprint methods for photonic structures. Figures are obtained from [58], [60], [61].

In general, nanoimprint lithography has been utilized in micropattern fabrication on colloidal nanoparticles indirectly. Recently, Pina-Hernandez and collaborators have proposed to use a commercial available high refractive index to pattern colloidal quantum dots via two different strategies.[58] As shown in Figure 9a, one strategy is to embed the titania sol-gel resist with 4% of quantum dots, which was then spin-coated on master molds prepared by electron beam lithography. The imprint was then conducted reversely onto glass substrate with higher adhesion to the resist. The other strategy is a two-step process, where the titania-based resist is reversely imprinted on glass first, followed by spin-coating of the QDs loaded PMMA. This work demonstrated sub-100 nm resolution, with high quality of the resulting photonic cavities as shown in Figure 9b (quality factor ~1000 for 1D gratings).

In addition, researchers working on bio-polymers have been utilizing nanoimprinting for advanced photonic structures. For example, nanocellulose film can be imprinted with arrays of micropillar, showing structural color feature.[59] Also, silk fibroin patterned with periodic nanoscale pattern have been demonstrated. To be specific, by controlling water content in silk, its glass transition temperature can be adjusted from 25 to 100^{o}C. Nanoimprinting can be operate at both room and elevated temperature, yielding high resolution photonic silk film(Figure 9c).[60] More recently, large scale nanoimprinting is achieved by integration with roll-to-roll method, and mass production potential is demonstrated on photonic crystals on hydroxypropyl-cellulose (HPC).[59], [61] For instance, 2D photonic structures with submicron periodic lattices have been reported(Figure 9d).[61] Besides the tunable structural colors, novel optical functionalities was demonstrated by

integrated with additional optically active component like dyes and plasmonic nanoparticles.

1.2.3 Combining top-down and bottom-up approaches

On one hand, bottom-up approaches are typically fast, convenient and cost-effective to produce photonic structures, thanks to the parallel process provided by self-assembly behaviours of the building blocks; however, these processes can only provide limited types of orderings and are sensitive to the processing conditions. On the other hand, while the top-down approaches demonstrate accurate control down to several nano-meters, with capability for arbitrary geometries, the scale-up production are not as promising as those by bottom-up approaches, due to the expensive instrumentations and typical serial fabrication process. Therefore, to have advantages from both worlds, people have been trying to integrate top-down approaches with bottom-up ones, with several successful demonstrations.[62], [63], [64], [65]

In general, two major strategies are applied to combine both approaches. (i) Self-assembly within pre-defined physical and/or chemical constraints via master molds fabricated via lithographic methods;[66], [67] (ii) selectively transfer self-assembled structures/patterns with the help of lithographic methods by transfer-printing/etching.[68], [69], [70]

For the first strategy, anisotropic alignment of nanocrystals with high aspect ratio in predefined physical confinement is a good example, demonstrating controlled birefringence behavior. Due to the elastomeric nature, biopolymer hydrogels are good candidate materials to be placed in physical confinements, where high level of orientational

alignment can be accommodated with large deformation.[71] For instance, within the mechanical confinement of microchannels in soft PDMS, silk fibroin could assemble into hierarchically organization with programmable morphology (Figure 10a).[72] In the microchannels, silk undergo β-sheet conformation/physical crosslinking during the fast filling-up and drying process, when permanent structural alignment of silk nanofibrils is induced by mechanical tension to PDMS substrate. Besides, strong birefringence-based structural color is yield from the highly aligned ordering of silk, which is programmable via the feature size and geometry of the PDMS mold.

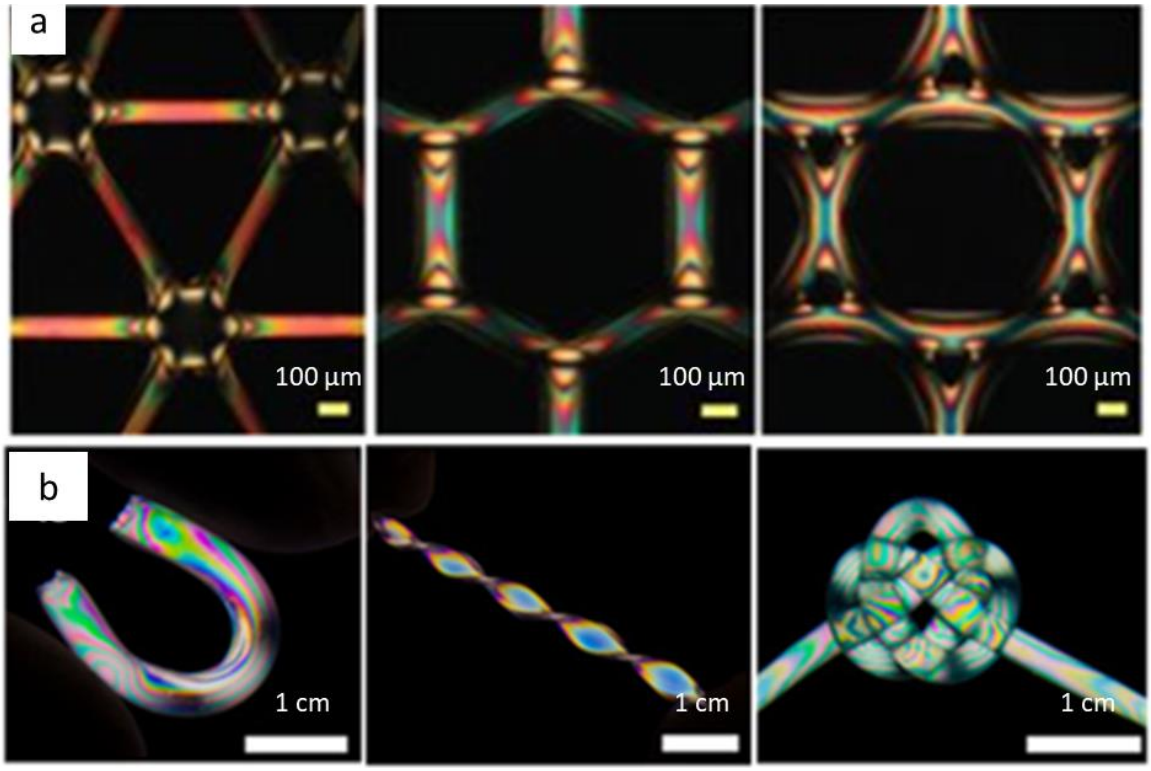

Figure 10 Self-assembly of soft materials in confinement with controlled optical properties. Figures are obtained from [72], [73].

Similarly, such top-down confinement is applied to cellulose hydrogels, while it is found that the isotropic-anisotropic transition can be induced by shearing force from the confinements.[73] As shown in Figure 10b, after the cellulose hydrogels is crosslinked in the physical confinement, the anisotropy under shearing force is visualized patterns of birefringent pattern.[71] Besides, because of volume shrinkage during drying, higher orientation degree is achieved from constrain on the motion of molecules. In general, assembly of both flexible 1D biopolymers nanofibers and stiff 1D nanocrystals can be controlled within soft polymer matrix confinement, defined with top-down methods.

As for the second strategy, various methods are developed, with difference in the technique utilized to transfer the self-assembled structure/pattern. For instance, intricate method is developed based on replica molding and subsequent photolithography, based on assembled 2D photonic crystal patterning. As shown in Figure 11a, after PDMS mold is replicated, it can be stretched to achieve unconventional orderings, the pattern is transferred onto photoresist layer by lithographic process, yielding a physical patterning where secondary colloidal assembly can be formed. [74] These methods can produce a wide range of unconventional 2D photonic crystals, including binary colloidal crystals (Figure 11b), nanohole array (Figure 11c), single/double lines, dimers, tilted dimers, zig-zag lines (Figure 11d) and zigzag rods (Figure 11e). Moreover, such combination of lithographic process and colloidal assembly extends the capability of colloidal-based nanofabrication methods, with great potential for flexible, robust and controllable patterning technique.

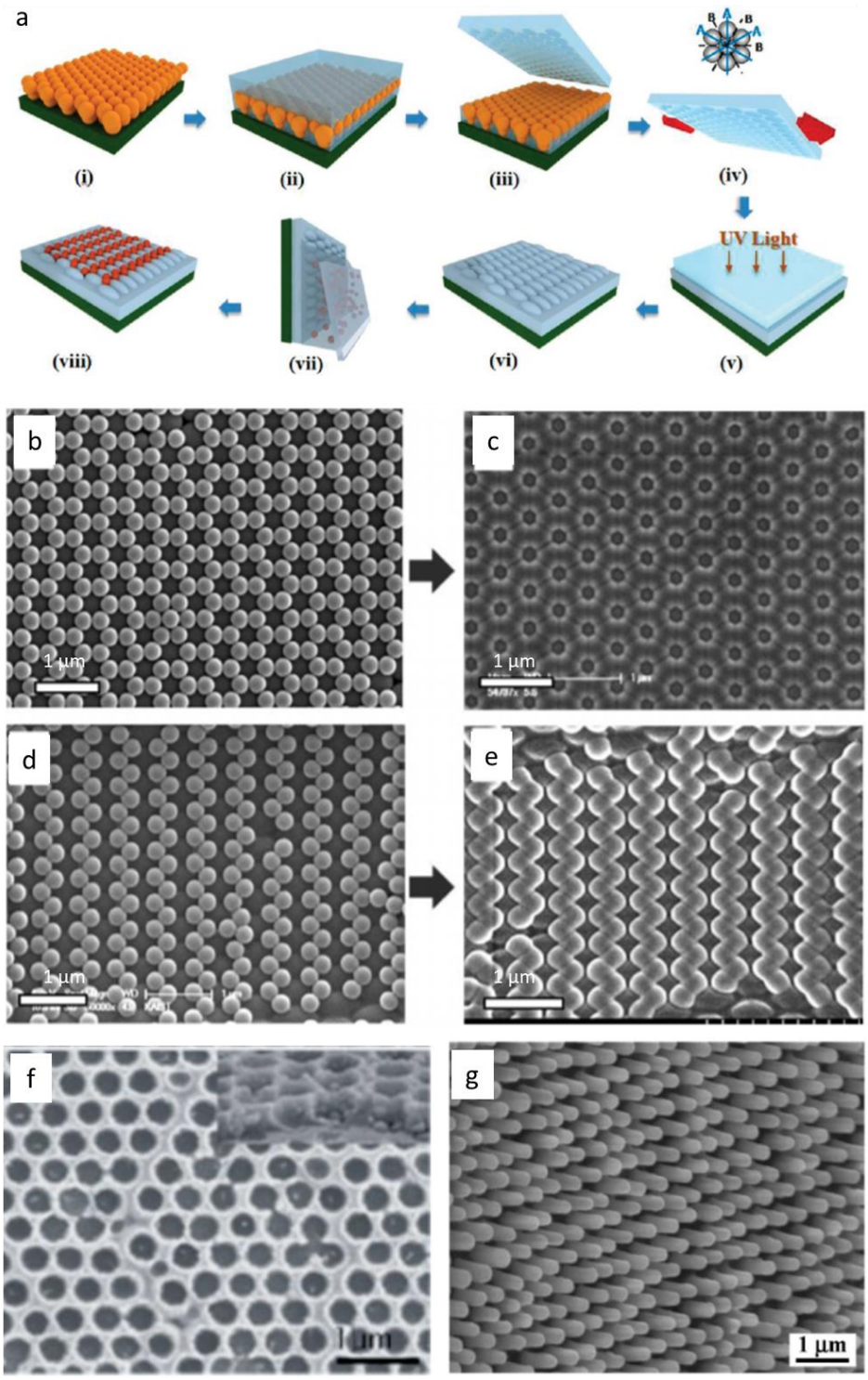

Figure 11 Transfer-printing and etching methods based on assembly of colloidal micro-particles. Figures are obtained from [74-76].

Another method takes advantage of photolithography and reactive ion etching (RIE) with assembled photonic crystals. For instance, photoresist particles is assembled on silicon wafer, and selectively exposed to solidify the periodic structure, after coating of silica and subsequent RIE etching steps with controlled etching depth, nano-holes could be formed in array of hexagonal organization.[75] The resulting pattern is shown in Figure 11f, which demonstrates a bowl-like morphology (cross-section). Besides, such method is applied on transfer non-close-packed colloidal crystals to underlying substrate.[76] As shown in Figure 11g, 2D photonic crystal structure is transformed from colloidal assembly into pillars with high aspect-ratio after series etching steps. The etched silicon can also function as template to transfer pattern to glass pillars with anti-reflection properties, with the help of PDMS molding and sol-gel synthesis.

1.3 Generation of chirality with cellulose nanocrystals

Microstructure of the chiral phase of CNC film affect the photonic properties profoundly, including the circular dichroism (chirality), photonic band gap width (specific color) and variation (color accuracy). Therefore, fundamental knowledge about the chemistry and derivation of CNC colloidal suspension, as well as influencing conditions during the self-assembly is vital to develop successful chiroptical materials from CNC.

In general, evaporation-induced self-assembly (EISA) of rod-like biopolymer is known to generate chiral nanostructures. Actually, several biopolymers nano-colloids assemble into chiral nematic liquid crystal phase when the concentration of dispersion reach certain level, such as fb virus,[77, 78] cellulose nanocrystals,[79] chitin nanocrystals,[80] and amyloid nanofibrils.[81] These biopolymers undergoes isotropic-nematic-cholesteric

phase transitions with increasing concentration during evaporation.[81] Such transition into cholesteric phase is typically evidenced by feature characteristic "fingerprint" texture, which is observable under polarized optical microscope (POM) when cholesteric phase is formed at final equilibrium stage (Figure 12).

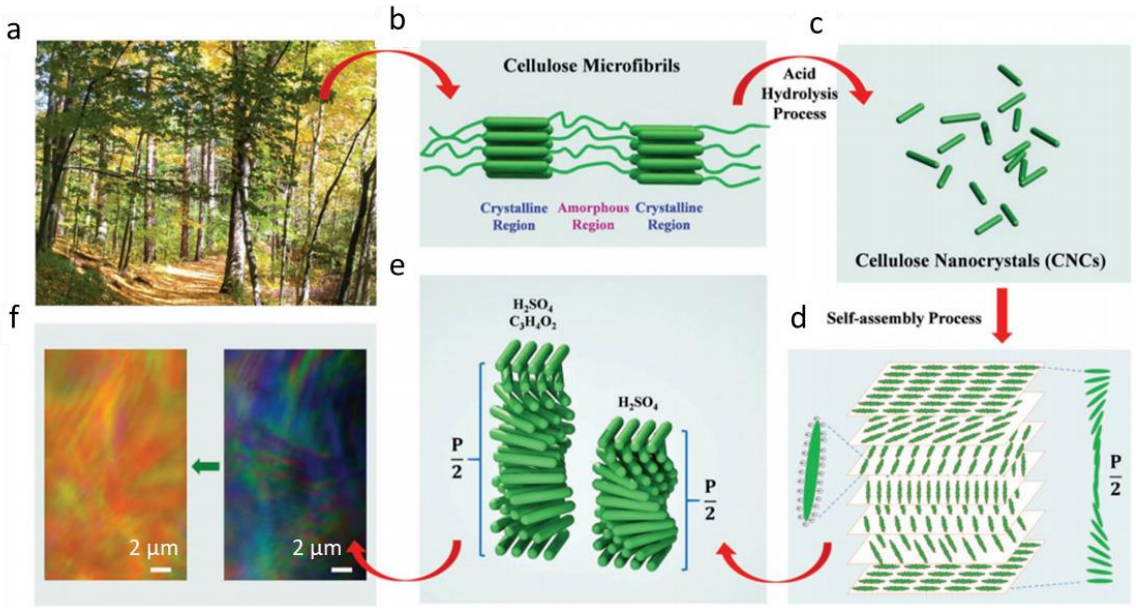

Figure 12 Derivation of cellulose nanocrystals from natural source and corresponding self-assembly into iridescent films. Figures are obtained from [84].

To date, however, only the CNCs films are reported to generate structural color. Unlike other biopolymers, the most striking property of the CNC liquid crystal (LC) phase is the preservation of chiral nematic structure into solid form after fully dried. Typical chiral nematic phases of CNC suspension have long-range order with pitch of helical structures ranging from 1 to 50 µm (Figure 12). As for fully dried film, the pitch decreases to submicron range (200 to 600 nm), enabling Bragg reflection in the visible spectrum thus the appearance of bright structural colors. Despite the vivid iridescence, stable position and width of reflection spectra is not easily obtainable, due to variance of pitch distances and orientations of domains of the cholesteric phases.[82]

1.3.1 Chemistry and derivation of Cellulose Nanocrystals (CNC)

Such variation in microstructure and photonic properties are inevitable from the multi-step derivation process of the colloidal CNC suspension from natural source. First, cellulose is separated from trees (Figure 12a), typically in the form of wood pulps. The amorphous regions of the native cellulose are removed during acid hydrolysis (Figure 12b), leaving the crystalline regions in the form of nanorods.[83], [84] The as prepared low concentration CNCs suspension distribute in the dispersion without any organization (Figure 12c). To form the desired chiral micro-structure of CNCs upon increasing concentration, phase transition from such isotropic to a cholesteric phase is the key. And two important aspects are demonstrated to affect the key transition process, one aspect is the length and aspect ratio of the CNC nanorods; the other is the surface potential of CNCs along with ions strength in aqueous dispersion.[85]

On one hand, the as prepared nanorods of CNC shows polydispersity in length and aspect ratio. For CNCs with higher aspect ratio, the onset phase transition concentration is expected to be lower.[86] To be specific, the onset concentration of CNCs derived from bacterial cellulose with aspect ratio of 44-73 is around 0.42 wt%,[87] while onset concentration of wood CNCs with aspect ratio of 34 is above 2 wt% .[88] As for the length, CNCs are less rigid when they are too long, causing the formation of nematic organization without the chirality, as exemplified by the TEMPO treated cellulose nanofibers (CNFs).[89]

Besides, phase separation occurs in polydispersed CNCs dispersion, where long CNCs self-organize into chiral nematic phase, while the shorter CNCs remain in isotropic phase.[87] More importantly, the aspect ratio affects distribution of pitch in final solid CNC

films. The pitch of the chiral phase in solution increases with the aspect ratio. Therefore, typical purification by dialysis and centrifugation is needed to improve the suspension with better uniformity of aspect ratio and length of individual CNC.[83]

On the other hand, because the self-assembly of the CNCs are mainly determined by balance between the attractive (hydrogen bonds and van der Waals forces) and repulsive interactions (steric and electrostatic interaction), it is feasible to manipulate the self-assembly by control the interactions chemically during the preparation of CNC suspension.[90] One specific method is to control the surface potential with modified surface functionality. For instance, with additional acrylic acid to the sulfuric acid in the acid hydrolysis step, carboxyl groups were introduced onto the CNCs surface along with the sulfate ester groups.[84] As a result, the CNCs are negatively-charged with a higher zeta potential (absolute value), producing stronger repulsive electrostatic force than CNCs obtained with hydrolysis by sulfuric acid only. The stronger repulsive interactions then yield helical CNC film with larger pitch distance (Figure 12 e), as demonstrated by the redshift of resulting iridescence (Figure 12 f).

Another effective method involves addition of electrolyte in suspension. Significant increase of the onset concentration is observed, when the counterions H^+ on CNC are replaced by larger ions such as Na^+, due to larger effective CNC diameter.[91] Actually, with the increase of counterions size, the critical concentration generally increases in the order of $H^+ < Na^+ < K^+ < Cs^+$.[92] However, addition of electrolyte have to avoid multivalent ions such as Al^{3+} and Mg^{2+}, which will generate ionic crosslink among CNCs, forming hydrogel with random networks and destroying any possible LC ordering.[93]

In summary, control of aspect ratio of individual CNC and chemical interactions is achievable during the hydrolysis and purification processes, which is essential in formation of solid CNC films with high microstructure uniformity and controlled photonic bandgap.

1.3.2 Control chiroptical properties of CNC

The optical chirality of CNC film is dominated by left-handed polarization. This is due to the structural dominance of left-handed helicoidal ordering. Such structural preference in handedness is evidenced by scanning electron microscope (SEM) characterization, one of the typical helicoidal Bouligand structures is shown in Figure 13a, demonstrating a pseudo-layered structure with left-handed twisted alignment of the nanocrystals. However, CNCs films demonstrating iridescence in both left-handed circularly polarized (LCP) and right-handed circularly polarized (RCP) channels are widely reported; even though the reflection observed in LCP channel is much stronger than that in RCP channel.[94], [95], [96] One of such comparison is shown in Figure 13b and c with obvious contrast in the blue iridescence. Such chiroptical response is partially related to the un-aligned multi-domain CNC liquid crystals structures, while the specific mechanism remains unclear.[95]

Beyond control over intrinsic properties of CNC suspension during preparation process as discussed in previous section 1.3.1, manipulation on the structural and optical properties is feasible via extrinsic methods like controlling evaporation conditions and adding external components to form composites with CNCs.

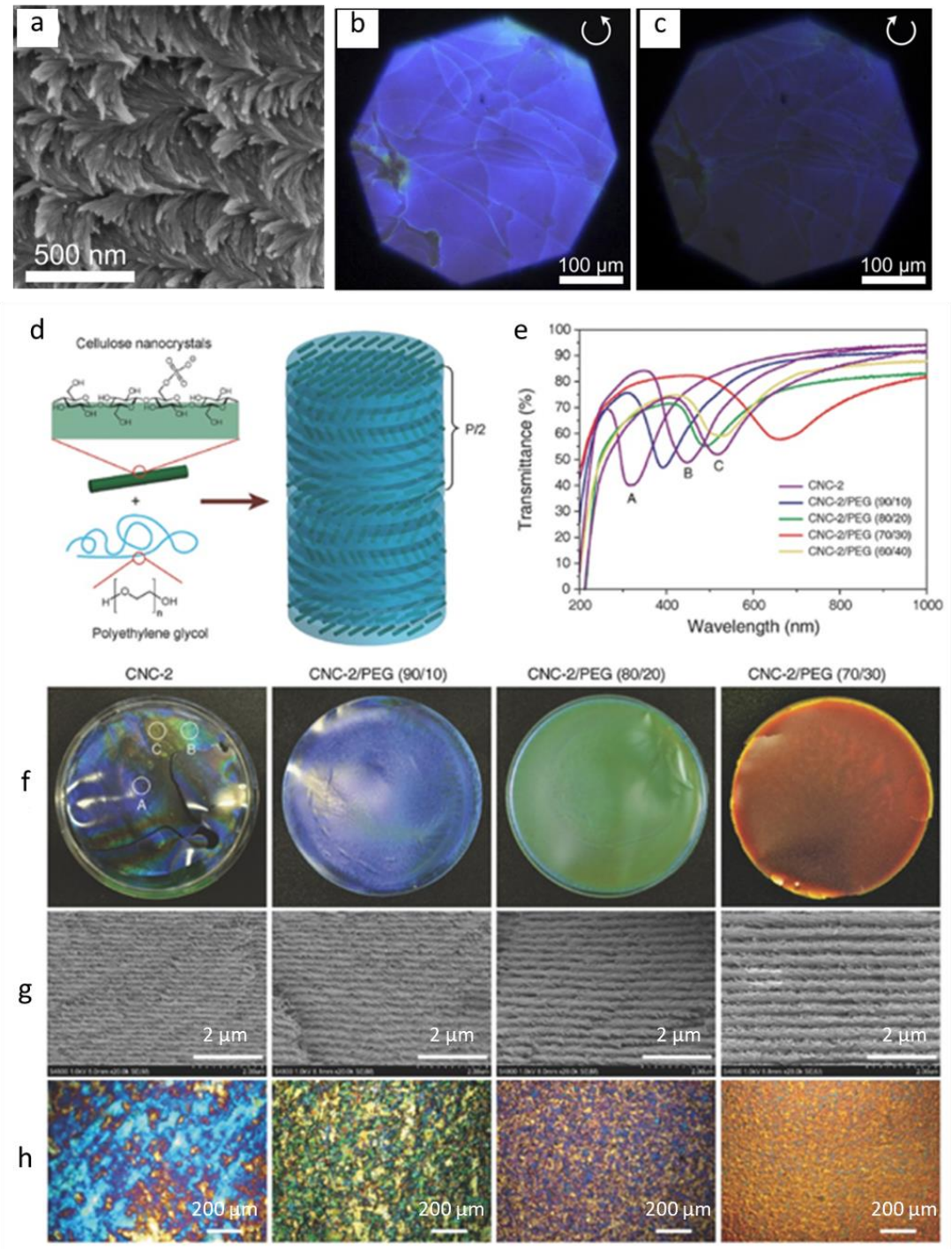

Figure 13 Controlled chiral structures of assembled cellulose nanocrystal and corresponding chiroptical properties. Figures are obtained from [94-96], [101].

As for evaporation conditions, such as humidity, temperature, wettability of substrates and magnetic field, all influence the uniformity and pitch distance of chiral structure to some degree.[97] A recent investigation assisted by cross-sectional observation of the phase transitions in nonspherical liquid crystal droplets reveals the impact of hydrophobicity of substrate on the evolution of LC tactoids.[98] In the case of hydrophobic substrate, the CNC tactoids firstly merge into continuous ordered phase under the upper liquid−air interface and then vertically spreads along the side face to the bottom. In contrast, the long-range ordered phase initially appears at the bottom center of the droplet and then horizontally spreads to the edge when evaporate on hydrophilic surface. The different dynamic behavior might be associated with the Marangoni flows, pinning effects and the interaction between substrate and CNCs.

Another popular method to manipulate the structural color is introducing external components. The pitch distance of the chiral structure can be easily regulated by controlling the amount of the external components. One type of components is soft water-soluble polymers. Various soft polymers, such as polyacrylate, poly(ethylene glycol) (PEG), and poly(vinyl alcohol) (PVA) have been introduced and co-assemble with CNCs to yield iridescent films.[99], [100], [101], [102] For example, CNCs can co-assemble with PEG, generating large-area flexible solid film with uniform structural color upon slow drying (Figure 13d).[101] This uniform structural color can be tuned in wide spectra range from blue to red *via* composition of CNCs and PEG (Figure 13e). With increasing PEG composition, the photonic bandgap of the film decreases, as evidenced by a redshift of the reflected color (Figure 13e, f). Microstructural characterization by SEM also supports this mechanism, as pitch distance increases with PEG composition (Figure 13g). Besides, good

affinity of PEG on CNCs is also demonstrated in the highly-ordered microstructure with uniform pitch distances and no defect (Figure 13g). Despite uniform structural color at macroscopic level, multi-color domains at microscopic level still exist with typical domain sizes at several tens of micrometers (Figure 13h).

Considering the intricate balance between attractive and repulsive interactions in CNC suspension, selection of soft polymers is very important for uniform chiral morphology. For instance, positively charged polymers are not suitable because the strong attractive electrostatic interaction with negatively charged CNCs will induced severe aggregation.

In addition to the composites method, a cellulose derivative, hydroxypropyl cellulose (HPC) provides alternative for self-assembling chiral photonic material. As a water-soluble cellulose ether with the advantages of low-cost industrial scale production, and non-toxic nature, HPC has been widely utilized in medical and food industries as colloidal stabilizers, flow modifiers and surfactants.[103] At high concentration (usually more than 50%), HPC aqueous solution can form chiral nematic ordered phase due to the chain stiffness.[104] The resulting films also show vivid iridescent structural color from Bragg reflections.[105] Manipulation of the reflection light wavelength is also achievable, as higher concentration leads structural blue-shift of structural color.[106]

1.3.3 Issues and potential with CNC as chiroptical material

As exemplified in previous discussion, one of the advantages of CNC films with chiral structure is the controllable pitch and structural color *via* several different means such as controlling the dimensions of nanocrystals, evaporation conditions and secondary

components. However, principles of how the chiral nematic LC phase are preserved in the solid state are still poorly understood, which limits more precise control over pitch distance and the alignment of the LC phase. Therefore, one of the frontier to develop CNC as chiroptical materials is to control the self-assembly behavior for uniform structural color not only at macroscopic scales, but also at the microscale. Assembling CNC LC phase in confined geometry in microscale have been demonstrated to be promising method to provide insight for controlling chiral organization.

For instance, Cherpak and co-workers obtained uniformly aligned chiral LC CNC structure *via* confined evaporation within thin capillaries.[107] The confinement enables tight control of fast and uniform birefringent CNC film formation, resulting in narrow optical reflection bands, which is beneficial for iridescence with higher color purity. Similarly, microfluidic devices are used to generate monodisperse CNCs microdroplets in oil.[108] This confinement by the water-oil interface allows the formation of an ordered chiral nematic shell. More recently, evaporation-speed has been proved to be critical for uniform structure and coloration of CNC films.[94] An outward capillary flow widely exists in conventional ambient evaporation condition. However, with an additional layer of hexadecane oil on top of the CNCs dispersion confined in micro-holes, the undesirable capillary flow is mitigated at significantly slower evaporation speed.[109] Even though all these methods demonstrate uniform chiral structural color at micro-level, their potential to scale-up for large-area CNC film with uniform structural color is uncertain.

In contrast with the uncertain future of these research focusing on the fundamental colloidal and interface behaviour of CNC suspension, several studies with more practical

emphasis has opened the horizon for CNC film as an advanced chiroptical materials, for generation of CP light both passively (chiral reflector), and actively (chiral fluorescence).

As for the passive method, inspired by the sandwich structures that reflect both left- and right-handed light in beetle, researchers infiltrate a layer of responsive nematic liquid crystal between two left-handed chiral namatic layers of CNCs, the middle layer function as a half-wave plate.[110] This unique photonic structure can generate both right and left circularly polarized light successfully, by tuning temperature and external electrical field.

In addition to switchable chirality, a recent development on passive generation of CP light focus on a broadband circular polarizer.[111] By adding anionic surfactant, considerable disorder with variation of helical pitch and axis orientations within domains are introduced deliberately. As a result, reflection in LCP channel is significantly broadend, as evidenced by the white reflection of such CNC film under natural light as well as contrast of reflection intensity between LCP and RCP light illumination (Figure 14a); besides, a flat absorption and broad CD spectra in Figure 14b. As for the microstructure, uniform distribution of small domains with birefringence is observed across the film under POM (Figure 14c). While conventional broad-band polarizers using birefringent crystals are bulky, such broadband circular polarizer based on CNC is compact and cost-effective.

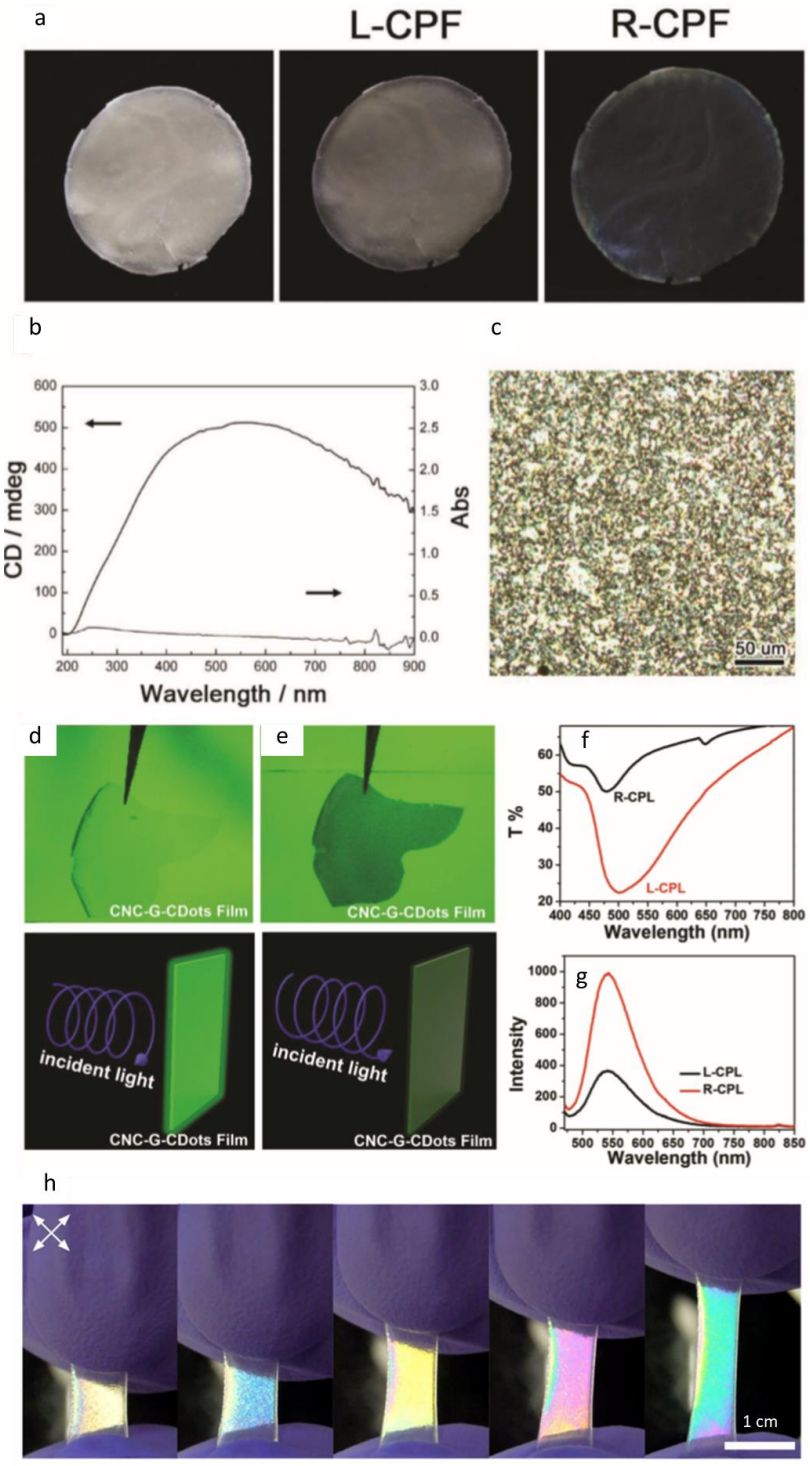

Figure 14 Recent developments on chiral optical applications of nanocellulose. Figures are obtained from [111], [113], [114].

The state-of-the-art for active generation of CP light utilizes carbon quantum dots as the fluorescent dopant, co-assembles with CNC in chiral structure.[112] The resulting films with retained chiral structure show asymmetric emission with stronger intensity in RCP channel. Such film with unique stimulated CP light is also demonstrated with the potential for detection of CP light.[113] As shown in Figure 14d, e, the film shows much stronger photoluminescence when the incident light is in RCP channel than with LCP channel. This is due to higher transmittance of light with RCP than LCP, as evidenced by spectra in Figure 14f, and the corresponding photoluminescence difference is quantitatively determined, as shown in Figure 14g.

Application beyond the CP light generation is also explored. For instance, with a combination of elastomer and CNC with chiral structure, large reversible deformations is accommodated while the strain level is revealed in the structure color.[114] Upon stretching, the color of the composite viewed between crossed polarizers changes sequentially from white to blue, yellow, pink and finally green, as shown in Figure 14h. The color changing property is attributed to reorientation of CNCs and unwinding of the chiral microstructure, which changes the birefringence. The composites show potential in novel sensor to visualize mechanical stresses in various structures.

1.3.4 Objectives of this work

As demonstrated in previous discussion, thanks to its nature abundance, environmentally benign and cost-effective preparation process, CNC with unique chiral structures induced by self-assembly process shows great potential for generation of CP light. However, despite recent development on CNCs as next generation of chiroptical

materials, several obstacles still exist on the way to fully release the potential. The challenge mainly comes from the nonuniformity of microstructures, where multidomains of tactoids varies in pitch and orientation of helical ordering. Such variance in microstructure not only hinders the generation of CP light with accurate and sharp coloration. Studies dealing with such challenge has demonstrate effective control with uniform ordering in micro-confinements, while still in need of the essential scale-up demonstration.

Therefore, to enhance the chiroptical properties of CNC film, a strategy to integrate photonic/optical structures in chiral CNC film is proposed. This strategy combines bottom-up and top-down fabrication method to take advantages of both worlds, especially controllability and scalability. On one hand, for bottom-up part, EISA of CNC will be optimized for preservation of the chiral structure of CNC with scale-up potential. On the other hand, photonic structures with precise design will be obtained and integrate with CNC by means of top-down lithography techniques. To be specific, several basic objectives should be achieved:

1. Successful integration of photonic/optical structures on CNC film surface, yielding free-standing film without distortion of the designed geometry in sub-micro level.
2. Functionality of the diffractive and refractive optical elements on CNC film, as expected by design.
3. Preservation of chiral stacking structure in CNC film, with good uniformity in macroscale.

4. Preservation of chiral optical property of CNC film, with strong circular dichroism and a dominant LCP light in reflection mode.

Besides, objectives at higher-level are also expected:

1. Enhancement on the coloration of generated CP light by CNC, including narrower spectral width, and controlled peak position.
2. Enhancement of the chirality of the CP light, possibly with higher asymmetric factor.

In conclusion, to fully release the potential of CNC as next generation materials for CP light generation, optical design/structures inspired by examples found in biological systems are selected and incorporated with CNC film with chiral structure.

In the following parts, integration with diffractive and refractive optical structures will be discussed in Chapter 2 and 3, respectively. In both chapters, sample preparation methods for corresponding structures (i.e. grating structures, 2D photonic crystals, and micro-lens array) will be described, followed by morphology and optical properties analysis in sequence. Discussion part focuses on the manipulation and enhancement of chiroptical properties, especially spectral feature and chirality. The last chapter will sum up current study with highlights in terms of both materials and methods developed in this study, followed by brief discussion for further developments and potential research directions in the future.

CHAPTER 2. DIFFRACTIVE OPTICAL STRUCTURES WITH NANOCELLULOSE FILM

2.1 Design of diffractive optical structures

2.1.1 Design of 1D diffractive grating structures

The 1D photonic crystal in the form of surface relief grating is selected, as it is a well-known photonic structure for convenient proof-of-concept. To match optical characterization set-up (e.g. range of incident and viewing angles, details in Appendix B2), simple simulation of the diffraction peak position with specific given angles are performed.

The calculation is based on Bragg equation and assuming Gaussian distribution of the light. For illumination (300 nm to 800 nm) at given incident angle θ_0 and observation angle θ_3, reflectance spectra were generated, assuming Gaussian distribution of the intensity around peak position. The simulated spectra have relative narrower width, comparing to the measured data, this discrepancy come from the dispersity of the intrinsic chiral structure as discussed before, which is not perfectly modelled with Gaussian distribution.

As shown in Figure 15a, for diffraction peak from grating structures at λ_g, [115] Then:

$$m\lambda_g = D \cdot (sin\theta_0 + sin\theta_3) \quad (7)$$

Where *m* is the mode number, *D* is the periodicity of the grating, and θ_0, θ_3 are incident angle and observation angle, with respect to film normal, respectively. As for Bragg reflection peak from intrinsic chiral nematic structure λ_c,[116], [117] one have:

$$m\lambda_c = n \cdot \frac{P}{2} \cdot (cos\,\theta_1 + cos\,\theta_2) \tag{8}$$

Where *m* is the mode number, *n* is the average refractive index of the CNC film (*n*=1.50), *P* is the pitch distance of the chiral structure, and θ_1, θ_2 are incident angle and observation angle, with respect to film normal, respectively. According to Snell's law, the four angles should meet with:

$$sin\theta_0 = n \cdot sin\,\theta_1 \tag{9}$$

$$sin\theta_3 = n \cdot sin\,\theta_2 \tag{10}$$

As a collective effect, one can calculate the peak position of CNC with extrinsic photonic structure, λ' with the following equation:

$$m\lambda' = D \cdot (sin\,\theta_0 + sin\,\theta_2) + n \cdot \frac{P}{2} \cdot (cos\,\theta_1 + cos\,\theta_2) \tag{11}$$

Based on equation 9 to 11, reflection spectra were simulated with Matlab and experimental values for refractive indices. Part of the simulated result for *D* ranging from 600 nm to 4000 nm, is shown in Figure 15b

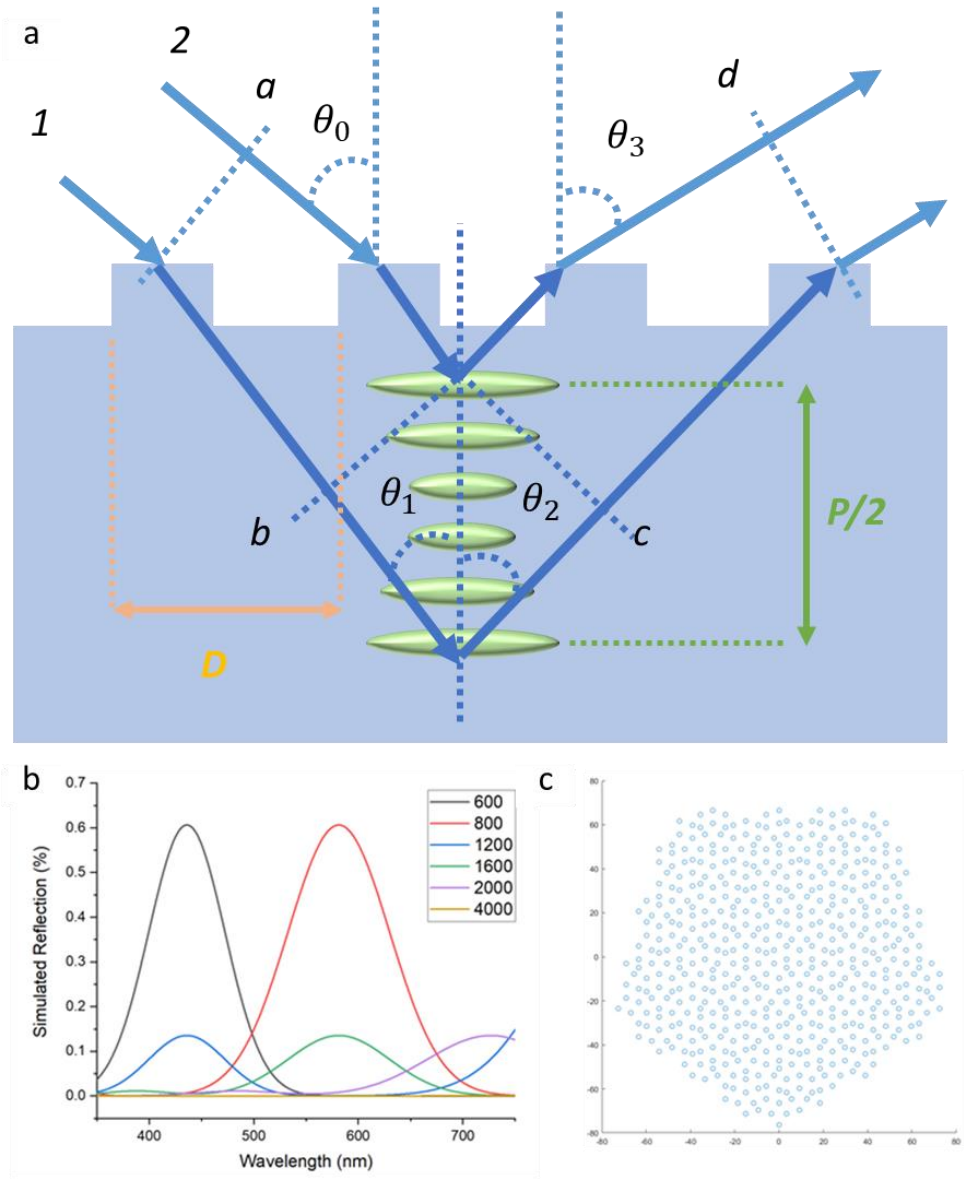

Figure 15 Design of 1D gratings and 2D photonic structures.

2.1.2 Design of 2D photonic crystal structures

As for 1D photonic structure on CNC film, the enhancement for optical property is limited in two aspects. First, the structural color is unidirectional, thus not effective when viewed along the long-axis of grating structure. Second, no physical confinement along

the trench is applied, leaving the potential of CNC assembly into more advanced photonic structures with higher dimensional complexity unexplored.

Therefore, besides 1D grating structures, integration of 2D photonic crystal is explored. In the design of 2D photonic crystals, structural coloration will appear the same in the same viewing cone, extending the viewing angle freedom, which overcomes the first limitation. To deal with the second limitation and probe the assembly within confinement at higher complexity, unlike typical photonic crystal with hexagonal or rectangular pattern, quasi-crystal pattern is chosen, which only possess 5-fold rotational symmetry, but no translational symmetry.[118],[119] Considering the needle-like anisotropy nature of CNC, such quasi-crystal confinement will disrupt any phase of CNC assembly originate from alignment. A matlab-generated quasicrystal pattern is shown in Figure 15c to shown the symmetry. Please be noted that only center part of the pattern is selected for clearance.

2.2 Fabrication process of diffractive optical structures

2.2.1 Fabrication of master molds

Both 1D surface diffractive grating structure and 2D quasi-crystal like pattern were defined with electron beam lithography. [120] The patterns were first generated in AutoCAD in two-dimensional images with precision down to 1 nm. Elionix ELS-G100 system was utilized to scan focused electron beam (100 keV) on spin-coated PMMA resist with thickness around 230 nm on regular Si wafer, at a dosage of 0.3 uC/cm2, and a spot-size of 1-10 nm, depending on the feature size. The PMMA at exposed area were developed off with a 1:1 mixture of methyl isobutyl ketone and isopropanol (IPA) with immersion and gentle shaking for two minutes and were rinsed with immersion in IPA and subsequent

gentle flow of IPA for about three minutes. Physical deposition of Cr on the sample was then conducted to reverse the pattern of etching mask on substrate. Mild plasma etching with O_2 and Ar was conducted at 150 W for 10 seconds to improve the adhesion of Cr on Si wafer. Subsequent coating of Cr was achieved via Denton-explorer e-beam evaporator at evaporation rate of 1 angstrom per second and final thickness at 50 nm.

The PMMA resist was removed by immersing in acetone solution for 5 to 10 mins and bath sonication for 30 seconds. As a result, the previous e-beam scanned areas were covered with Cr while the remaining areas were bare Si wafer. Inductively coupled plasma (ICP) etching was then conducted on Si wafer with Plasma Therm ICP. The Cr on pattern areas act as etching mask, while Cl_2 and Ar gas were utilized as chemical and physical etchant with etching rate of Si at 11 nm per seconds for 3 to 5 minutes, to produce a feature height around 200 nm to 350 nm. The Cr was then removed by immersing in Cr-etchant for 2 minutes and rinsing with distilled water for 3 minutes. The as prepared Si molds were either directly used for film preparation or modified to be hydrophobic before prior to drop-casting of CNC suspension. For the surface modification, the Si molds were first etched with air plasma at low power (50 W) for 60 seconds, and then moved to a desiccator immediately. 5 microliter of trichloro(1H,1H,2H,2H-perfluorooctyl)silane is dropped on petri-dish in the same desiccator, and the desiccator is pumped down to vacuum with mechanical pump for 10 minutes and the molds were kept in vacuum with the silane for an hour at room temperature.[121] The self-assembled perfluorosilane modified the surface wettability from hydrophilic to hydrophobic, as contact angle increase from 57 to 108 (Figure 28g).

Photolithography and reactive ion etching were utilized to prepare extra diffraction array pattern with larger feature size.[122] First, photoresist SPR-220 was spin coated and baked before UV-light exposure. Photomask with arrays of rectangles with a series of periodicities was used to define the pattern. TSA-MA6 mask aligner were used for UV exposure at contact mode with i-line. The pattern were developed with resist-developer MF-315 for 3 minutes and rinsed with deionized (DI) water. The as defined pattern on photoresist layer was transferred into Si wafer by etching with gaseous CHCl3 and Ar in Plasma Therm RIE etcher for 10 minutes. The resulted etching depth is around 150 nm. The remaining photoresist were then removed by piranha solution and as-prepared mold demonstrated hydrophilic surface. The molds were then modified to be hydrophobic utilizing the same method with perfluorosilane as described before.

2.2.2 Pattern-transfer on CNC films

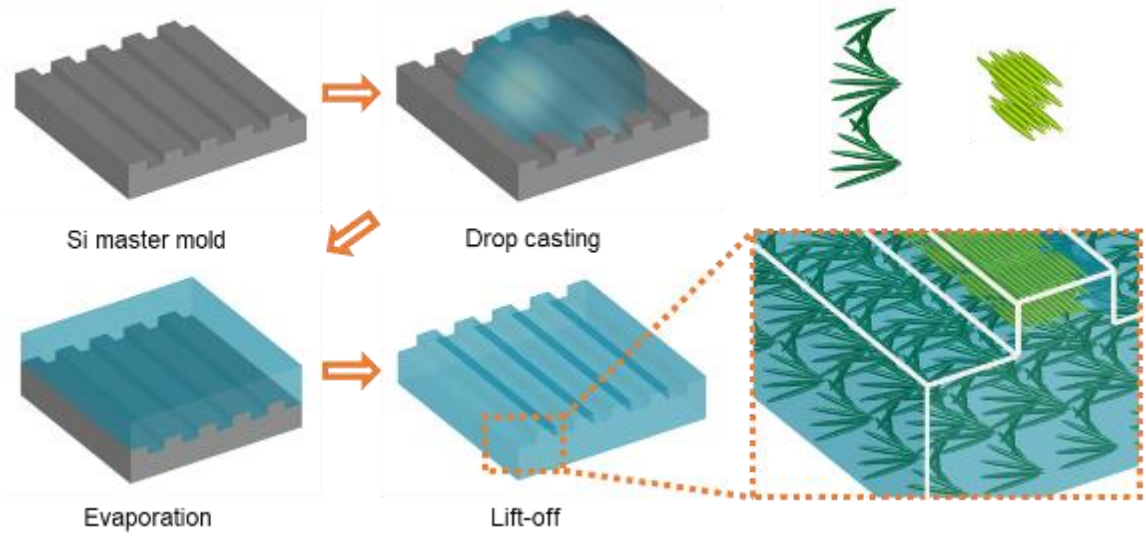

Figure 16 Fabrication process to integrate surface optical structures on CNC films.

With obtained molds with hydrophobic surface, CNC suspension was then drop-cast on the mold and kept at room temperature (22 degree C) and 40% relative humidity in

fume hood, with flow rate of air around 0.6 m/s for 9-10 hours. After water evaporated, CNCs assembled into solid film, which could be pealed-off from the mold easily. The process of replica molding is shown in Figure 16. As for a successful molded sample, microscopic ordering of CNCs on surface and in the bulk are observed (Figure 28 in Appendix B1), the enlarged schematic in Figure 16 represents highly aligned ordering on surface and chiral nematic ordering in the bulk film, respectively.

2.3 Morphology of self-assembled CNC in optical structures

2.3.1 Morphology of CNC with grating structures

The high quality of extrinsic photonic structures of pure CNC is evidenced by topography scan using atomic force microscopy (AFM). AFM images across large area revealed that periodicities and height contrast are both well registered from the corresponding master molds (Figure 17a). The uniformity of pure CNCs gratings is quite good, as defects like small cavities, and glitches existed at low density (Figure 27). To directly prove the existence of chiral nematic structure, scanning electron microscopy (SEM) images were taken at the film cross-section. Periodic layers relative parallel to the film were clearly seen, where spindle-shaped CNCs were highly aligned in plane, and the orientation of neighboring layers were rotated continuously in a left-handed manner. Two typical cross-section SEM images are shown in Figure 17b.

Extrinsic photonic structure can be utilized to manipulate the generated CP light in terms of wavelength and propagation direction. However, design and implementation of new extrinsic photonic or optical structures for additional functionality should take account

of the highly-anisotropic nature of the CNCs, especially its influence on the capability to self-assemble into complex nanostructures.

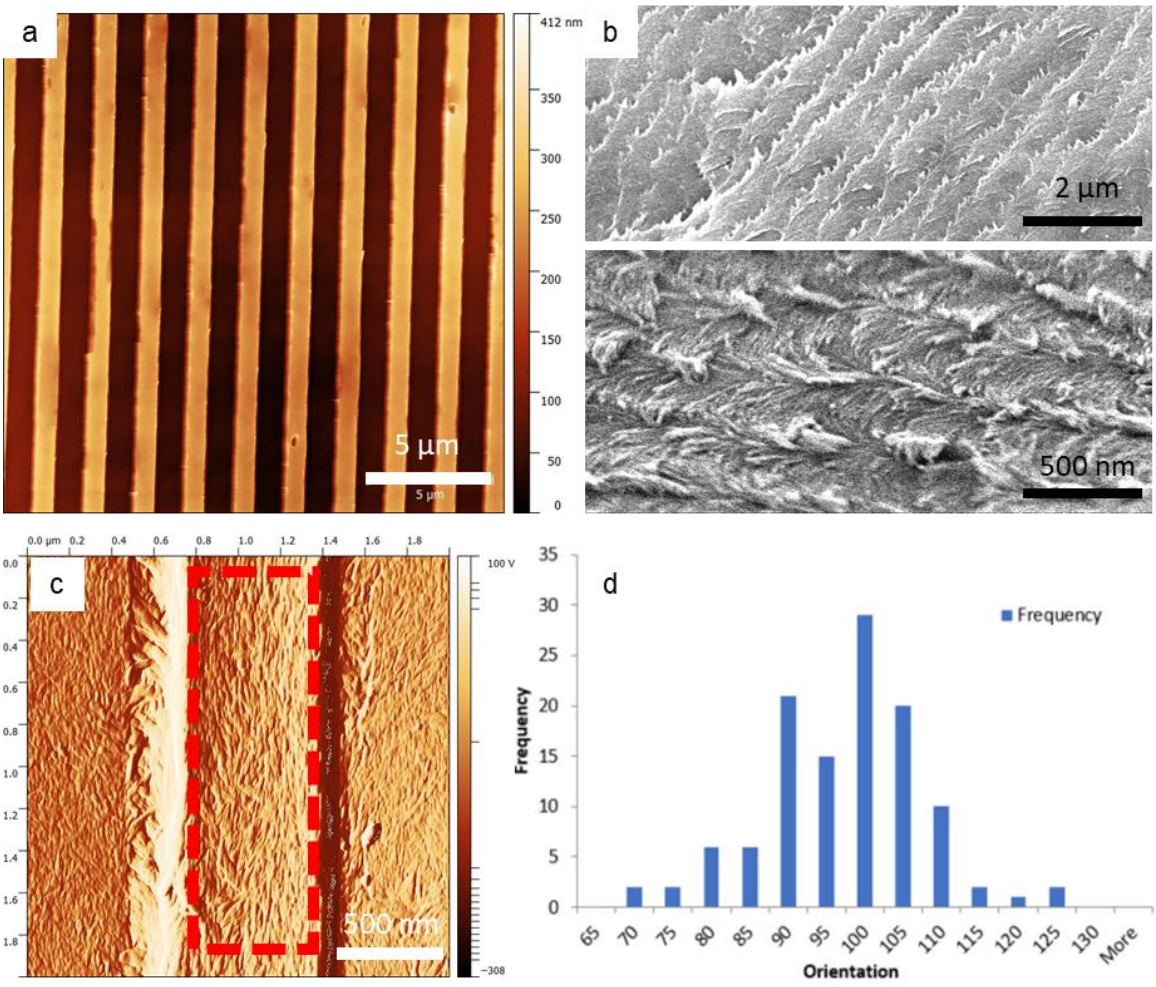

Figure 17 Surface and cross-section morphology of CNC with optical structures (gratings).

Therefore, to gain fundamental knowledge about the assembly within photonic crystals, it is important to study the morphology of the CNC films with different confinement condition. During the evaporation-induced assembly, capillary force and thermal Marangoni flow are influenced greatly by surface tension between substrate and CNC solution, as reported in previous study.[98] Therefore, surface energy is chosen as one

parameter for this morphology study. By chemical modification of the Si master mold to be hydrophilic or hydrophobic (Figure 28g), providing opportunity to probe the difference in assembly behavior. Therefore, replica molding was performed on both silanized Si mold, and non-silanized Si mold. Instead of being free-standing like CNC films from hydrophobic molds, films from the hydrophilic molds were pealed-off with the help tape. From topography scanning by AFM, hydrophobic mold yielded good registration of the mold feature, with well aligned orientation of CNCs along the receding micro-trenches of the gratings, while CNCs on the protruding part of the gratings showed less ordering in orientation (Figure 28). Notice that the protruding part of the molded CNC films were under confinement from side wall of mold during the self-assembly.

CNCs on patterned surface are aligned along the confinement trench. The orientation of CNCs shows Gaussian distribution centered at 0° (along with trench), while the deviation (σ) value decreases from ±13.3° to ±8.4° when confinement narrows from about 690 nm to about 280 nm (Figure 17c, d). The corresponding orientational order parameters (calculation in Appendix D) increase from a very high value, 0.89 (at 690 nm confinement width), to even higher value of 0.97 (at 280 nm confinement width), while the ordering parameter for surface without confinement is only about 0.207 (Figure 28f). In comparison, capillary tube/osmotic-induced orientation is close to 0.8,[95], [123] and doctor blade fabrication results in CNC alignment with orientation parameter close to 0.9.[90]

Such high local orientation can create surface-tighten birefringence contribution to mediate light interaction with less organized interior materials.[95], [124] The CNC film cross-section shows well-aligned morphology confirming the chiral organization and

further supporting the aforementioned notion of the presence of the unidirectional CNC alignment only within ultrathin topmost layer (Figure 17c).[98], [96]

As for the underlying mechanism, the alignment of CNC resembles the naturally occurring nematic phase of CNC, which is formed before formation of chiral nematic phase, during the increasing of CNC concentration. The nematic phase tends to evolve into chiral nematic phase to lower internal energy, however, the repelling force from the physical confinement hindered such thermodynamically driven phase-transformation. To reduce the surface tension with the micro-sized mold, CNCs assembly took the highly aligned ordering. In contrast, even though physical confinement was the same as in hydrophobic molds, hydrophilic molds has higher affinity to CNCs thus lower surface tension. Surface layer of CNCs in contact with the mold were strongly attached to the mold, with less freedom to re-orient or phase-transform, resulting in a more random orientation. As for poorer registration of feature and defects at surface, they were probably introduced at the pealing off process, where part of the film, or the grating structure were remained on the mold.

2.3.2 Morphology of CNC with 2D photonic crystals structures

Even though CNCs showed good conformal molding from the gratings structure down to 350 nm, the rod-like nature of CNC may still post limitation to the formation into other photonic structures.[94] On one hand, to determine the lower limit of the confinement size, mold with arrays of nanoholes from diameter of 0.4 μm to 2 μm were fabricated, with

a depth around 250 nm. On the other hand, to avoid specific orientation of CNC structure on surface photonic structure, the pattern should has higher order of symmetry than four-fold rotation. In this case, molds with nano-pillars in pen-rose pattern were fabricated for the incorporation of 2D photonic crystal structures on CNC.[119] The photonic patterns with 5-fold symmetry have been successfully replicated on CNC at different lattice constant, ranging from 200 nm to 800 nm, with 20 nm intervals (Figure 18 c, d).

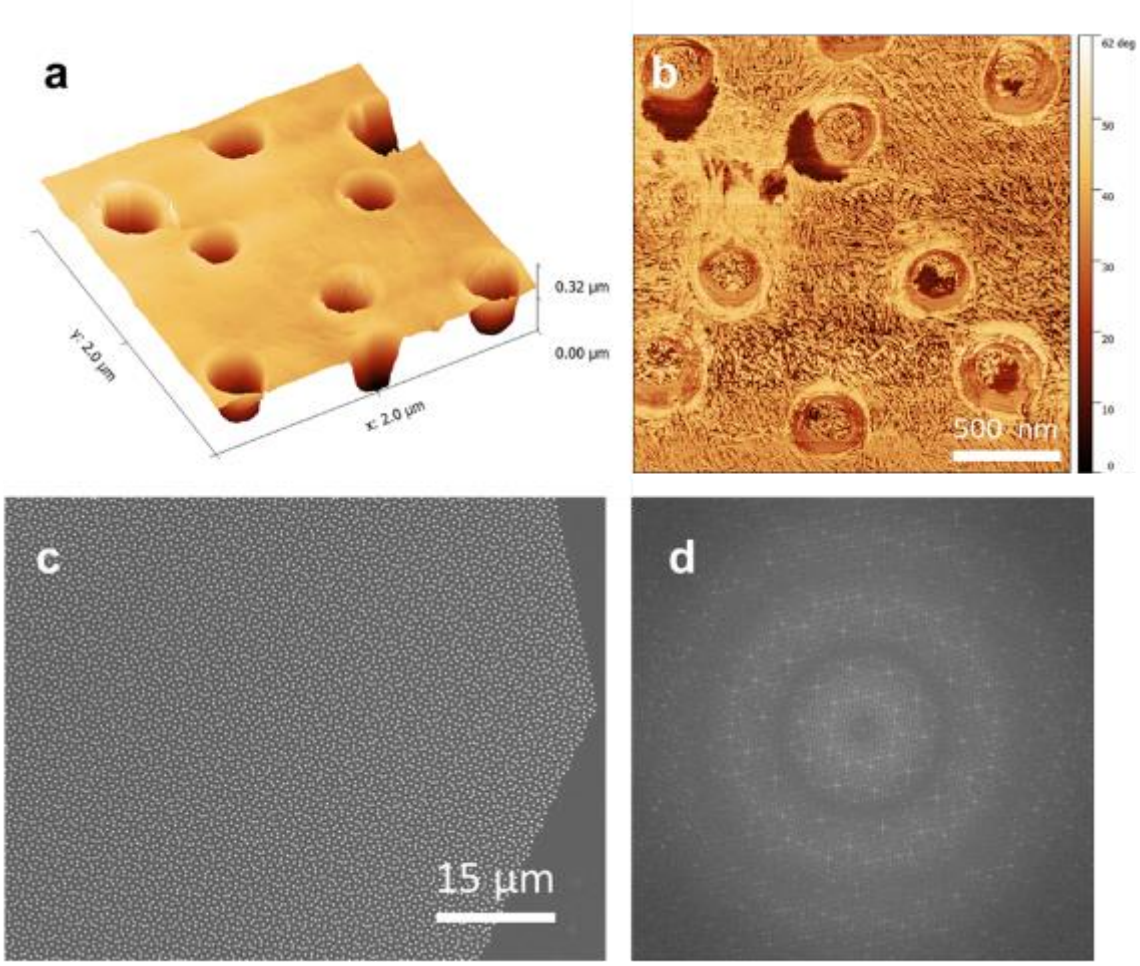

Figure 18 Surface morphology and pattern of CNC with 2D photonic crystals.

As shown in the zoom-in AFM image (Figure 18 a), the CNC film possesses very smooth and integrity surface without any microcracks existed around the photonic holes. The depth of the nano-holes is about 200 to 250 nm, with good uniformity (Figure 18a).

At a closer look in the phase image, the assembly of CNCs doesn't have preferred orientation, while formed conformal feature surrounding the nano-pillar confinements (Figure 18b). Even at the spacing between two adjacent pillars where the free space is about 190 nm, CNCs can assemble into solid structure without any void or dislocation (Figure 18b). Such conformal assembly with nanoconfinements proves the capability of CNCs to form complex nano-structure smaller than its length, indicate the potential for more advanced photonic structures from chiral CNC. Similar to the grating case, this is formed as a result of reduction of interface energy.

In addition to quasi-crystal pattern, to further test the capability of the incorporation of extrinsic photonic/optical structures, extra diffraction optical elements were chosen as a test-structure. In this test, shallow micropillars with four-fold symmetry is fabricated. It is designed with larger spacing between micropillars, so that the orientation of surface layer of CNC won't take specific orientation to produce unwanted birefringence.

2.4 Optical Properties of CNC with diffractive optical structures

2.4.1 Optical properties of CNC with grating

Based on the optimized molding process, artificial photonic structures were successfully incorporated on pure CNC films, with preserved intrinsic chiral nematic structure. The coexistence of the two photonic structures was directly observable. Under daylight illumination, the obtained film showed bluish iridescence throughout the whole film, indicating the existence of chiral nematic structure. While more vivid, highly viewing-angle-dependent structure color demonstrated the presence of uniform grating structures (Figure 19a).

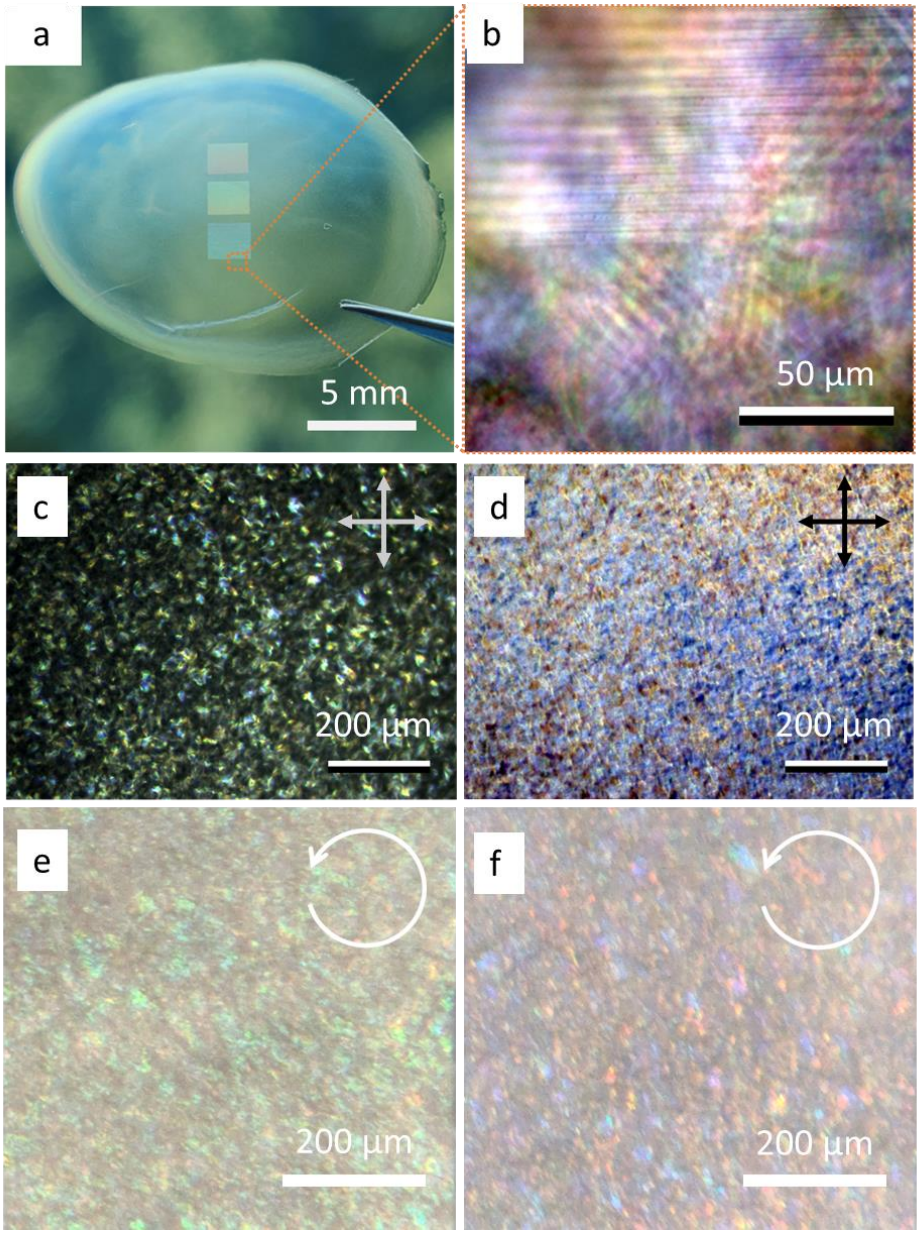

Figure 19 Optical properties of CNC with optical structures (gratings).

At closer look under polarized optical microscope (POM), fingerprint features with different spacings and directions could be observed, indicating orientation variations of the chiral nematic structures (Figure 19b). Besides, domains displaying various colors could be observed under both dark-field and bright-field (Figure 19c, d). These domains are sized around several tens of microns. Their coloration spans the whole visible range from

red to purple, while mostly located in blue-purple region (Figure 19b, e, f). Such multi-domain and fingerprint features has no observable difference between flat CNC areas and photonic-structure patterned areas, supporting the assumption that the chiral nematic structures are well-preserved.[82], [95] The extrinsic gratings are also observable with the POM, with weaker optical contrast due to the shallow depth (250 nm) of the gratings. Figure 19b showed the grating area (top half) along with flat area (bottom half) next to it. It is worth noticing that the underlying fingerprint features are continuous regardless of whether the film surface is flat or patterned, indicating minimal to no impact of surface physical confinement to the ordering of CNCs in bulk film.

2.4.2 Enhancement of chirality with grating

The combination of intrinsic and extrinsic photonic structures results in enhanced optical property. The unique left CP light is generated from the chiral nematic structure, while the extrinsic gratings re-shaped the spectra of CP light with narrower and tunable peak. As demonstrated in Figure 20a, gratings structure with 1.6 μm periodicity was incorporated on CNC film. Stereo-microscope images of the grating area under white light illumination with specific incident angle are collected with three different conditions: direct observation without any polarizer, with left-handed polarizer inserted in the light path of reflected light, and with right-handed polarizer inserted in the light path for LCP and RCP observations, respectively.

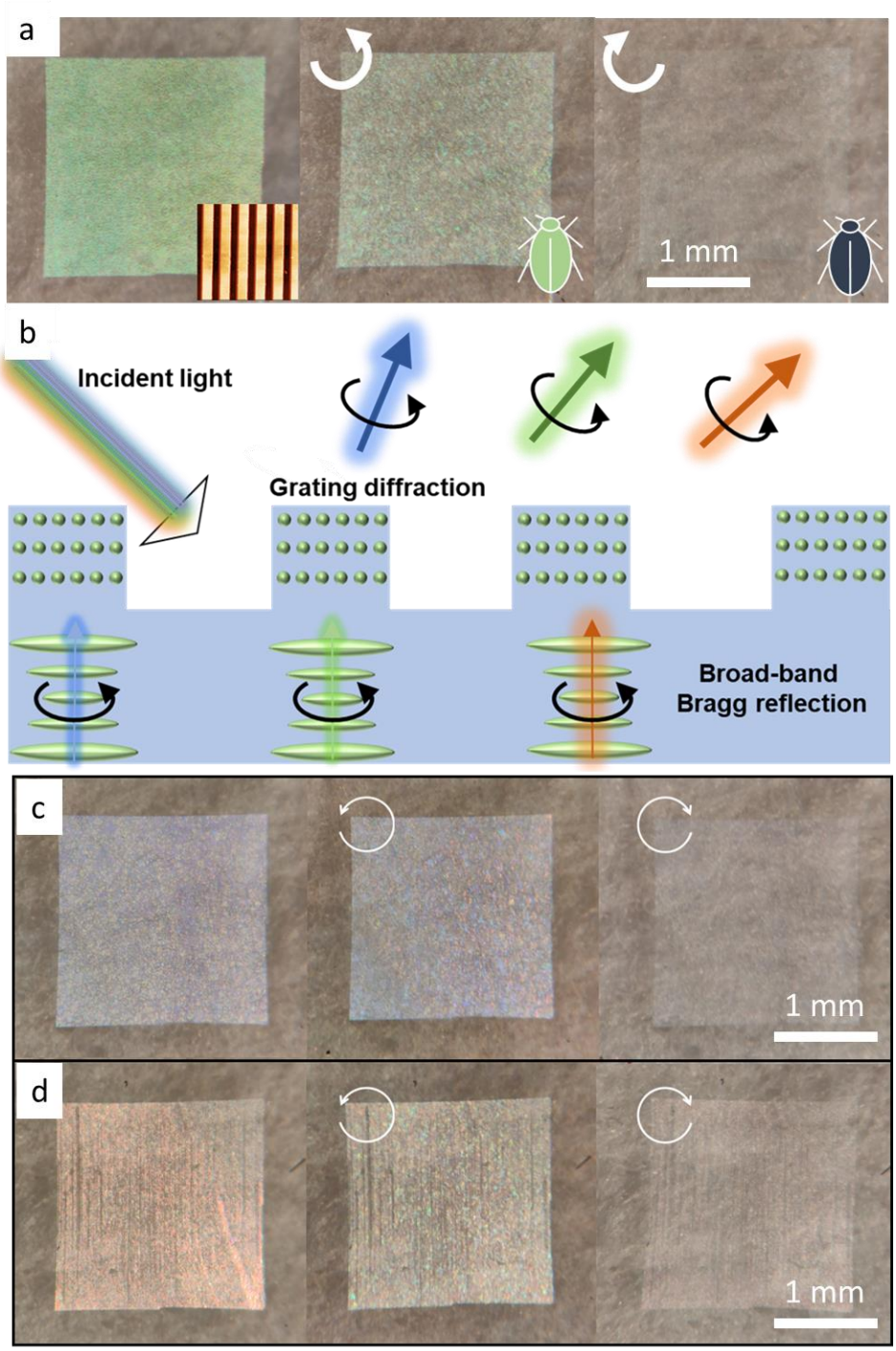

Figure 20 Circularly polarized light generation and enhancement from CNC integrated with grating structures.

Three major contrasts are observed at first look. First, compared to gray surrounding area without pattern, patterned area reflects vivid green color. Second, the reflected coloration could go thorough left-handed polarizer but not right-handed one. Third, the intensity of the reflection is reduced when left-handed polarizer is inserted, comparing to direct observation. The first contrast reveals the role of the extrinsic photonic structure in narrowing the spectra for constructive diffraction. The second reveals the role of intrinsic chiral nematic structure as endowing reflected light in left-handed polarization. The third contrast is rationalized by the low transmittance of the polarizer film (40% at visible wavelength, spectra in Figure 31 in Appendix B2). At closer look at the image with left-handed polarizer, small domains of various colors including red and blue become noticeable in the grating area, while most of them are green. Such diversity in enhanced coloration is a collective effect, as reflection is first generated by the domains in chiral nematic film, and then enhanced by the surface gratings.

To be specific, the reflection color can be controlled by the grating periodicity from blue to red, while the chirality of reflection and multidomain remain the same (Figure 20c, d). While the enhanced circular dichroism of the patterned CNC films is easily observable in the reflection mode, it is hard to quantify the reflection spectra in circularly polarized channel due to signal attenuation and background noise. Nonetheless, accurate quantitative measurement can be done in transmittance mode with optical fiber (Figure 29b), to quantify the CD, the asymmetric factor is calculated from equation 12.[134]

$$g = \frac{(I_L - I_{\mathrm{R}})}{(I_L + I_R)/2} \tag{12}$$

Where g is the asymmetric factor, I_L is the light intensity with left-handed polarization while I_R is the light intensity with right-handed polarization.

Table 1 Asymmetric factor of transmitted light through CNC with and without surface patterning.

Color	Position*	Wavelength (nm)	$g_{pattern}$**	g_{flat}**	Enhancement ratio for g
Red Laser* **	Peak	656	-0.91	-0.087	10.5
Red	Peak	614	-0.31	-0.11	2.8
	Band edge	538	-0.46	-0.16	3
Green	Peak	550	-0.21	-0.15	1.4
	Band edge	468	-0.33	-0.22	1.5
Blue	Peak	484	-0.18	-0.21	0.9
	Band edge	418	-0.2	-0.24	0.8

Note: * Data from intensity of light transmitted and diffracted by gratings on CNC film, also plot in Figure 31, peak and band edge positions are determined for each diffraction peak, separately.

**** $g_{pattern}$ is asymmetric factor of surfaced patterned CNC, g_{flat} is asymmetric factor of flat CNC without pattern, both are calculated by eqn. 1.**

***** Red laser utilized as light source in this measurement, pattern of CNC in this measurement is micro-lens.**

The result is listed in Table 1. Original plain CNC films have an asymmetric factor ranges from -0.05 to -0.25 at wavelength range in the range of 400 nm to 750 nm indicating modest asymmetry CD transmission in CNC films with random tactoid morphology (Figure 31 and Table 1). As for the CNC film with surface optical gratings, $g_{pattern}$ shows significant, manifold increase with g values ranging from -0.18 to -0.46 in the range of 418

nm to 614 nm (Table 1). Interestingly, while the circular dichroism (|g|) of original CNC film is higher at blue region and gradually decreases with increasing wavelength; the patterned CNC shows higher asymmetry at longer wavelength (Figure 31).

This trend of chirality is attributed to the increase of light path inside chiral structure, because light with longer wavelength is diffracted with a larger angle. As a result, the enhancement asymmetry factor (ratio of g values in areas with gratings to the areas plain areas) is found to be about 3 for red light (614-656 nm), about 1.5 for green light (538-550 nm), but show some decrease at blue light (418-484 nm).

Overall, these values of asymmetric factor, generated in the passive method (through light transmittance), are two magnitudes higher than those generated with active approach (with fluorescence enhancement) with chiral molecules or assembly of dye in chiral nanotubes, which, moreover, are centered around emission bands.[125] These high asymmetry is comparable with other active methods with blend of chiral molecules in polymer (0.2-0.5), complex of chiral ligand capped lanthanide complexes (0.1-0.5), carbon quantum dot doped cellulose nanocrystal film (-0.74) (Table 2 in Appendix C) [126],[127],[113],[128], and close to the value in passive way with cellulose nanocrystal (-0.87). Comparing to other strategies, such strong chirality across a relatively wide range within visible wavelengths is achieved in thin film of surface engineered pure CNC materials, without complication of adding emissive materials, thus demonstrating potential for broadband generation of highly asymmetrical chiral polarization light.

The mechanism in generating CP light with enhanced coloration is depicted in Figure 20b. Inside the solid CNC film, tactoids of chiral nematic phase differ in orientation

and the pitch distance.[129] Such multidomain nature of the CNC film, produces pixelated structure color in one single film. To be specific, when CNC film surface is flat, a wide range of wavelength of light could meet the Bragg diffraction condition even at fixed incident angle and viewing angle.[21] Therefore, a broad-band reflection of CP light is generated without prominent structure color. When extrinsic photonic gratings are incorporated on the surface of CNC film, however, the film produces vivid coloration. In this case of combined photonic structure, after traveling through and being diffracted by the surface grating layer, incident light is then Bragg reflected and endowed with LCP by the chiral nematic phase. The CP light with mixed wavelength is finally diffracted by the surface grating, resulting in color dispersion with preserved polarization. As a result, the generated CP light is enhanced with narrower wavelength range. To be specific, intrinsic CNC film showed broad band reflection spectrum across the visible region, with peak around 480 nm, and a full width at half maximum (FWHM) around 300 nm. As for CNC film with surface photonic gratings, the FWHM are narrowed to be 200 to 250 nm, with tunable peak position spans from 410 nm to 560 nm. Reflectance spectra from both flat and surface-patterned CNC film are shown in Figure 31.

The CP light generation mechanism is verified with circular dichroism (CD) spectroscopy of the film. The measured CD spectra was plotted together with reflectance spectra of flat CNC film at 90 degree in Figure 31. CD spectra shows the difference of transmittance light with LCP and RCP, it includes the contribution from both the reflection and absorption of light. The prominent positive peak confirms the generation of left-handed CP light by CNC film, while the similarity of the two spectra in peak shape and

position also support the observation that the major component of reflected light is left-handed CP light.

The proposed mechanism is also supported by simulation result (Figure 31).[115] Based on calculation of the collective light path differences from both extrinsic and intrinsic photonic structure, the peak position of CP light could be solved. The simulated spectra have relative narrower width, comparing to the measured data, this discrepancy come from the dispersity of the intrinsic chiral nematic structure, which is not perfectly modelled with Gaussian distribution.

2.4.3 Control wavelength with 2D photonic crystals

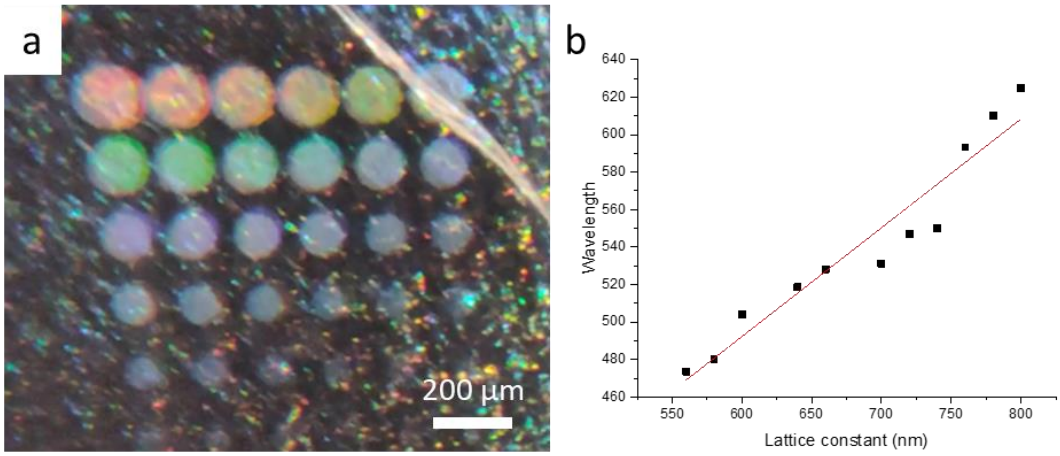

Figure 21 Tunable optical properties of CNC integrated with 2D photonic crystals.

The spectra-shifting by the presence of photonic structures, if well-designed, could function as a wavelength selection filter on top of broad-band chiral-selective reflection from the intrinsic chiral structures. In this case, CNC film can generate CP light with desirable wavelength. However, due to birefringence of CNC, aligned structure at the gratings would endow linear polarization to the light passing through or reflected from the

structure, which will weaken the unique circular dichroism from the chiral nematic phase, to avoid such negative effect on the optical property, two-dimensional photonic crystal is a better choice to incorporate.

As for the 2D photonic crystals with quasi-crystal pattern, under illumination from oblique angles, gradual redshift of structure color with increase of lattice constant was observed, as shown in the stereo-microscope image in Figure 21a. Due to the conformal assembly into 2D photonic structure, the patterned chiral CNC film exhibits vivid structural color as compared to the surrounding flat area. The flat CNC region shows pixelated coloration under white light illumination (Figure 21a), which comes from the chiral structures with variation among domains. However, CNC film shows uniform coloration within the photonic area. More important than the color uniformity, controlled wavelength shift of structural color via with changing lattice constant is demonstrated. As shown in first 3 rows of patterned area (Figure 21a), with increase of lattice constant from 520 nm to 800 nm, the reflected color shift gradually from violet to red. As expected, such structural color is angle-dependent, when the illumination angle increases, resulting in changes of diffraction mode and exact primary wavelength. The peak wavelength of the structural color from different pattern regions is plotted versus the lattice constant shown in Figure 21b. The good linear fitting between reflection wavelength and lattice constant suggests effective enhancement of chiral CNC generated CP light with tunable coloration. Combined with the preserved chirality, this control over wavelength indicates the potential for programmable enhancement of the CNC generated CP light.

2.4.4 Light diffraction with preserved chirality

As for the larger micro-sized diffraction structures, with the help of red diode laser. diffraction pattern from both array of micro-pillars in four-fold symmetry (Figure 22a) are compared with that from one-dimensional gratings (Figure 22b). Specific optical set-up is shown in Figure 30a, where light source is generated from a common diode laser, and the laser light first passes thought CNC film, with the optical structures on the side facing the laser. The observation of diffraction pattern in LCP and RCP channels are realized by inserting circular polarizer film with left- and right-handed polarization, respectively. It is worth noticing that, the quarter-wave plate side of the polarizer film is identified and faces the incident light. The receiving plate for the laser pattern is a black film, to enhance the contrast of bright spots in observation.

On one hand, the transmitted laser shows chirality with a dominance in RCP than LCP. As the diffraction pattern were collected through no polarizer, through left-handed polarizer and right-handed polarizers, separately. As expected from the presence of chiral nematic structure, the transmitted light from both 2D (Figure 22a) and 1D (Figure 22b) diffractive structures show stronger contribution from RCP than LCP, as LCP light underwent Bragg reflection in the left-handed helical structure throughout the film.

On the other hand, the diffraction pattern is obtained with good uniformity across large scale, evidenced by the diffraction patterns with clear diffraction spots at higher angles, as shown in Figure 22c. Besides, increasing periodicity from 4 μm to 32 μm, the distance between adjacent modes of diffraction changes reciprocally, which obeys the diffraction equation exactly.

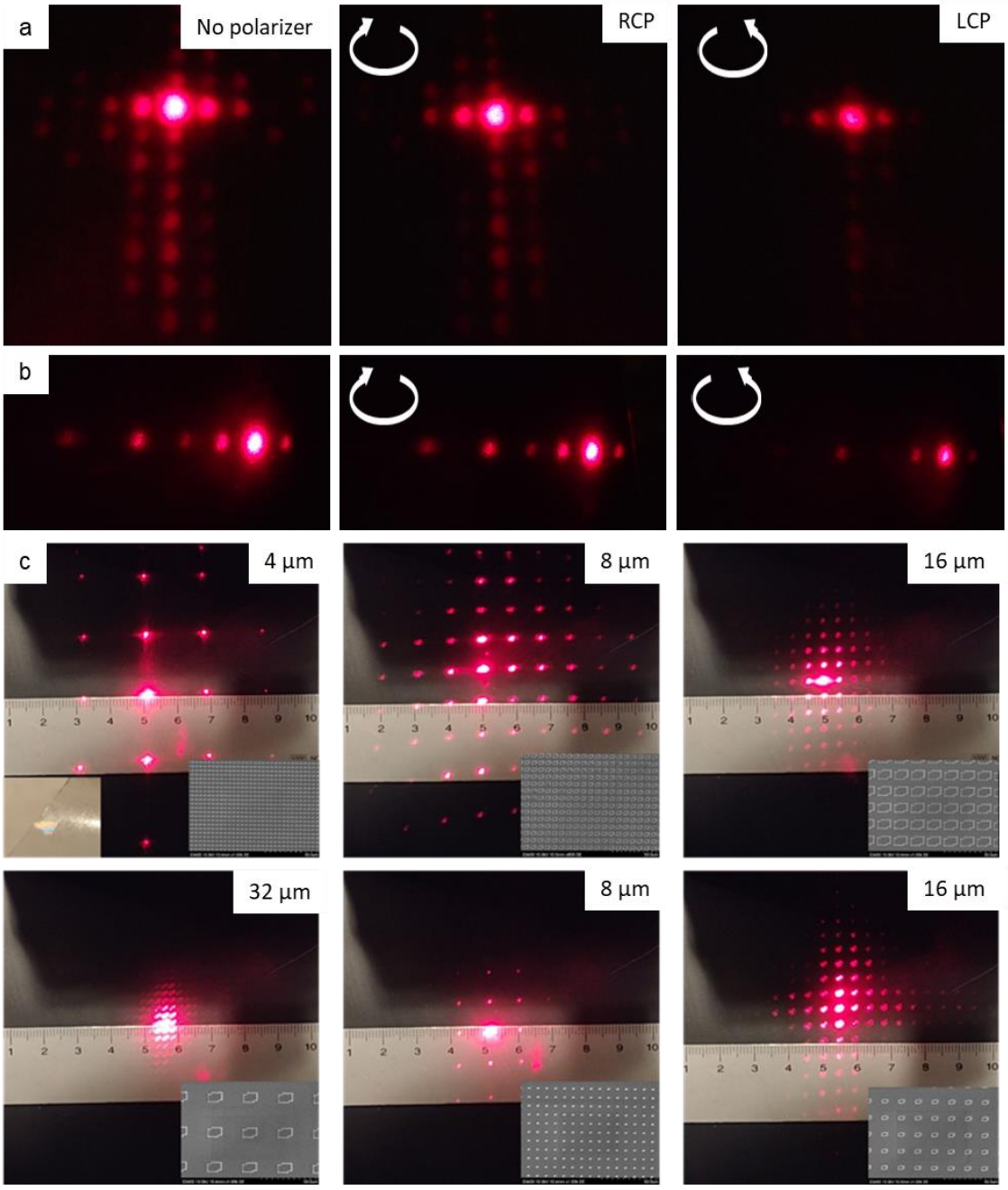

Figure 22 Light diffraction properties and chirality through CNC with integrated diffraction patterns.

2.5 Summary on CNC with diffractive optical structures

Based on the morphological and optical studies, with both good preservation of the chiral structure and successful registration of diffractive optical structures, patterned CNC films possess great potential to extend the optical functionality of generated CP light. Actually, both 1D grating structures, 2D photonic crystal with quasi-crystal pattern and 2D diffractive pattern with micro-sized periodicity are integrated on freestanding CNC film. The conformal assembly into confinement down to 190 nm results in successful physical replica free from distortion of the original photonic structure. Such good registration and uniformity of morphology produces uniform structure color, as well as tunability by the periodicity of the gratings or 2D photonic crystals. More importantly, the diffractive functionality also enhanced the chirality of the generated CP light significantly, with increase of asymmetric factor up to three times. All in all, the extrinsic surface diffractive optical structures could possibly function as color-filter to reshape the spectra of broad-band CP light from the intrinsic chiral structures, along with enhanced circular dichroism, especially at wavelengths away from the band-gap defined by intrinsic chiral stacking structure.

CHAPTER 3. REFRACTIVE OPTICAL STRUCTURES WITH NANOCELLULOSE FILM

3.1 Design of refractive micro-lens array

In addition to enhancing CP light with respect to spectra width and position, control over propagation directionality is beneficial for generated CP light. As discussed in session 1.1. 3, learning from nature, one effective optical structure to prove this possibility is micro-lens array.

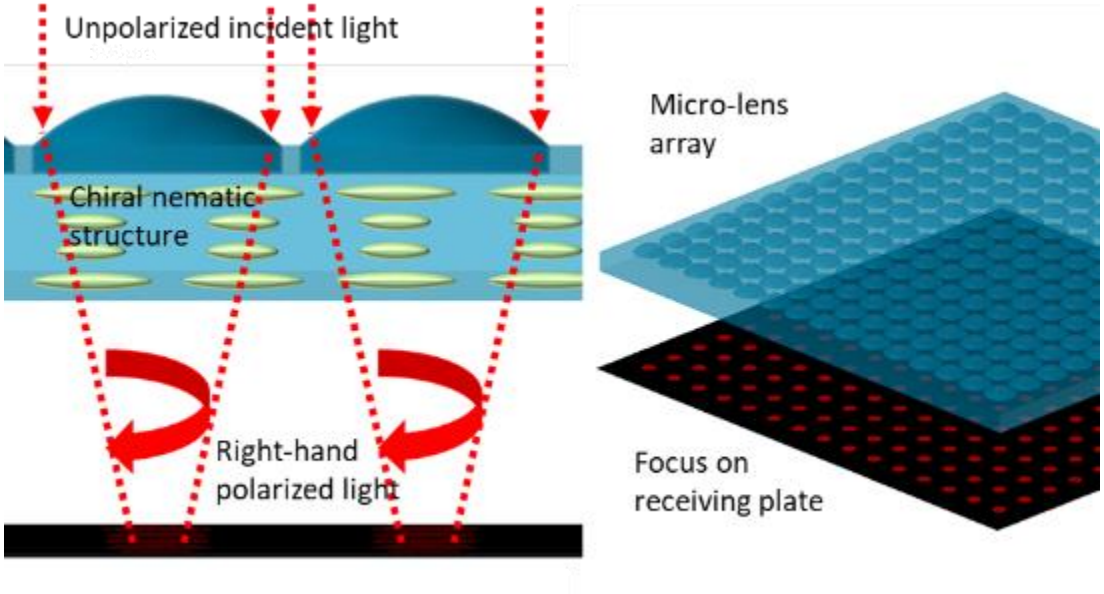

Figure 23 Design of micro-lens array on CNC film.

In the design of micro-lens, incident light beam parallel to the optical axis will be focused through the refractive micro-lens (Figure 23). When these micro-lenses are arranged in an array on the same plane, they not only focus the light to increase the signal intensity, but also provide a wider angular acceptance to reduce reflection and increase transmittance. Ideally, integration of 3D micro-lens array on chiral CNC with tailored

geometries can provide CP light more functionality for possible applications in advanced imaging system.[130]

To be specific, micro-lenses first focus the incoming light beam, while the chiral structure endows chirality to the transmitted light.[128] The designed light path is sketched in Figure 23. According to the lens equations 6, effective focal length of the resulting micro-lenses will be determined by parameters including refractive index, radius of the micro-lens, and the total thickness of the structure. The refractive index of CNC is about 1.5 to 1.52, while the dimensions of micro-lens is set to be 0.2 mm, with a cap-shape cut from 60 degree of latitude on the sphere. The thickness of the film can be controlled down to 0.1 mm, by controlling the volume of original CNC colloidal suspension with known weight percentage. The resultant effective focal length is about 0.4 mm.

3.2 Introduce micro-lens on CNC film

Preparation of the molds for microlens array utilized two-photon 3D lithography and subsequent PDMS molding. Nanoscribe GT was utilized to define the microlens geometry, by focusing 780 nm laser into the IP-dip photoresist and polymerize regions corresponding to the AutoCAD model.[131] The scan of laser was set through a 23X objective and in galvo (reflecting mirror) mode, with a speed about 10 mm/s. The array of micro-lenses was anchored on perfluorosilane modified Si wafer and the whole substrates were immersed in SU8 developer for 20 minutes and rinsed with IPA for 2 minutes, following the scanning.

The as prepared microlenses were molded by PDMS molding. Sylgard 184 from Electron Microscopy Sciences were used to mold the reversed geometry. The molding was

assisted by vacuum pumping in desiccator to remove bubbles and the curing was done at 60 °C in oven for two hours. The PDMS molds were then released from the Si mold with micro-lenses successfully. The as-prepared PDMS mold is ready for drop-casting of CNC suspension.

The evaporation of CNC suspension was performed by direct drop-cast on mold with reversed geometry (cavities). The conditions of self-assembly is the same as that for surface grating structures, with room temperature at 22 °C, relative humidity at 40% and flow rate of air around 0.6 m/s in a fume-hood. After all water evaporated overnight, CNCs assembled into a piece of solid film, which could be pealed-off from the mold easily, due to the hydrophobic nature of the PDMS.

3.3 Properties of micro-lens array

3.3.1 Morphology of CNC with micro-lens

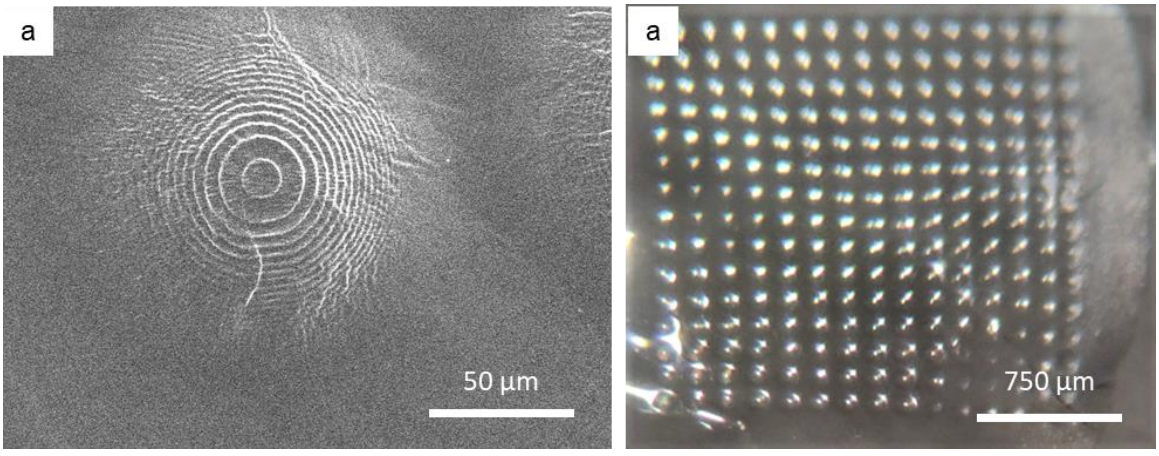

Figure 24 Morphology of micro-lens array integrated on CNC film.

The micro-lens structures are successfully integrated on CNC film. At a closer look with SEM, the confocal-ring features on the micro-lens were shown on the molded CNC,

which come from the scan pitch of the lithography process. While small defects are observed on the micro-lens, the general good registration of geometry at high resolution (Figure 24a).

At a larger scale, the micro-lenses are well organized in the array. The film is more transparent under white light, compared to the film with diffractive structures, due to reduced thickness (Figure 24b). The morphology check confirms that the designed geometry is well translated into a functional optical element on CNC film.

3.3.2 Optical properties of CNC with micro-lens array

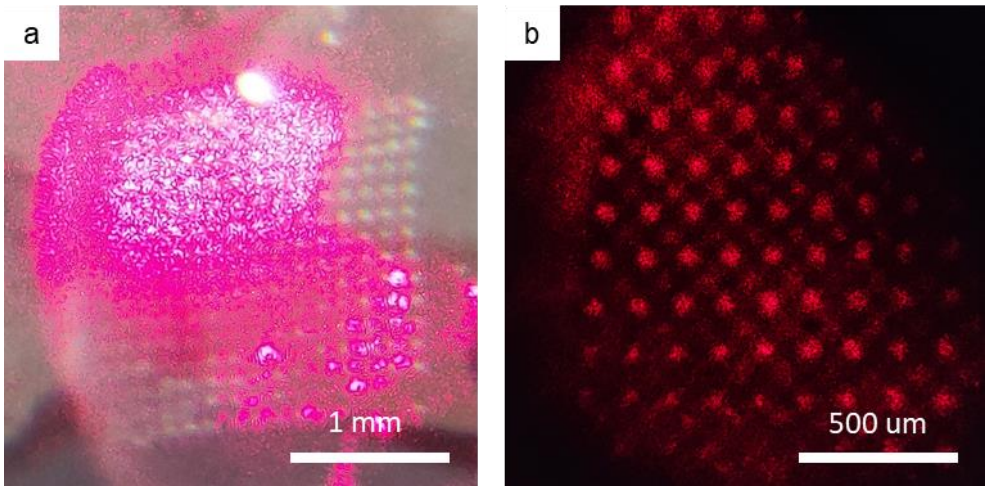

Figure 25 Optical property of CNC film with integrated micro-lens array.

The light-focusing function of micro-lens is tested in a similar set-up with that used in light diffraction test (Figure 30a). By placing the micro-lens array facing to the incoming laser beam (Figure 23a, Figure 25a), the large laser spot is split and focused to form an array of smaller, brighter spots on the focal plane (Figure 25b). The comparison of laser spot size and the size of micro-lens array is shown in Figure 25a. In the resulting pattern of focused spots on the black receiving plate, each bright red spot was focused via

individual micro-lens, separately; while the secondary, dimmer spots were formed from imperfect alignment of the light path and the natural curvature of the film.

The light-twisting power of the film with micro-lens is also demonstrated with diode laser. Intensity of transmitted light through the film was measured directly, through additional left-handed polarizer and right-handed polarizer, separately. Specific optical set-up for quantitative measurement is shown in Figure 30b. To be specific, red laser generated from a common diode laser pen passes thought CNC film, with the array of micro-lenses on the side facing the laser. The measurement of transmitted light intensity in LCP and RCP channels are realized by placing circular polarizers accordingly. An optical fiber connected with spectrometer is used to detect the spectra.

As plotted in Figure 31, the light transmitted through CNC film has a dominance in RCP. The asymmetric factor, as determined by the equation 12, is extremely high, with a value about -0.91 ± 0.08 at 636 nm. This very strong circular dichroism is higher than recent studies, where g value is about -0.87 to -0.51 (Table S2).[113], [128] Besides, a very high enhancement of asymmetric factor compared to original CNC film at 10 times is also observed.

3.4 Summary on CNC with refractive micro-lens structures

In conclusion, we developed a facile and efficient approach to integrate micro-lens array, onto freely standing chiral CNC films. This one-step fabrication approach combined top-down lithography (two photon lithography) with self-assembly of CNC, which allows for the construction of well-organized optical structure into array. The resulting freestanding CNC film exhibits significantly enhanced CP light with high increase of

asymmetric factor up to 10 times at 636 nm. The normal focusing function is also tested. This integration method provides a simple and convenient strategy to modulate the flow of CP light directly from CNC with compact form factor, indicating potential application in advanced detection or imaging systems for CP light.

CHAPTER 4. CONCLUSION AND OUTLOOK

4.1 Major conclusions of current study

In conclusion, by a strategy with combination of top-down lithographic methods and bottom-up assembly of cellulose nanocrystals (CNC), we demonstrate successful integration of both diffractive and refractive optical structures with CNC film with chiral structures. The major issue of nonuniformity of structure coloration due to intrinsic variance of CNC is mitigated with introduction of extrinsic optical structures on the film surface. Significant enhancement of the optical properties in terms of spectra, chirality and propagation obtained also opened a new pathway to develop CNC as advanced chiroptical materials.

To be specific, several objectives are accomplished in this study. Including i) preservation of the chiral stacking structure with high circular dichroism, ii) good registration of several optical structures with various symmetry and geometry at high precision across several length scale, iii) compact form as robust free-standing film.

More importantly, significant improvements in several aspects are achieved with these engineered bio-photonic films. As for the coloration, the diffractive grating structure and 2D quasi-crystal structure exhibit brilliant and controllable structural colors. The spectra are reshaped by the surface gratings with narrower width by about 50 to 100 nm. The angle-dependent iridescent is widely tunable with pre-designed periodicity of the optical structures. In comparison with other complex methods, such manipulation with

artificial structures shows comparable range and effectiveness, with much better repeatability and simpler process.

Interestingly, enhancement of circular dichroism is observed in broadband range extending from blue to red spectral colors, with high absolute value of asymmetric factor up to 0.91, and an enhancement factor up to 10. Comparing to other studies in literatures, such broadband enhancement in asymmetric factor is quite unique, especially in long wavelength of visible range. Finally, the concept of possible refractive functionality with CNC is proved for the first time, *via* the micro-lens array system. This demonstration lays a foundation for further development of CNC into functional optical elements.

Beyond properties of materials, this strategy has been demonstrated to be a facile and efficient approach to integrate various dimensional extrinsic optical elements at multi-length scales, including surface diffractive grating, photonic crystals and micro-lens array, into freely standing chiral CNC films. The one-step fabrication approach combines advantages from both top-down lithography and self-assembly of CNC, enabling the construction of well-organized photonic structures with critical dimension down to 190 nm. This integration strategy provides a simple and convenient strategy to modulate the spectra and propagation of CP light directly from CNC, free from complications like control over self-assembly with additional materials like crosslinker or chemical modifications.

4.2 Potential and ongoing developments

Looking ahead, with the enhanced chirality and obtained manipulation over optical properties, such chiral CNC film with extrinsic optical structures will find its application

in biologically active chiral optics, including chiral light generation, chirality sensors, colorimetric biosensing, stereoscopic display, chiral imaging system, and polarization encoding.

However, to fully release the potential of CNC as next generation chiroptical materials, especially for the generation of CP light, further endeavor is needed in several aspects: i) incorporation of optically active materials like fluorescent dye or quantum dots, to extend the CP light generation from a passive method to active method; ii) optimization of the photonic structures, especially implementation at a larger scale, along with design principles to tailor the structure with various coupling-out method of generated CP light in specific devices or application scenarios; iii) large-scale production-compatible methods to improve uniformity at microscales, ideally with well-aligned domains or even single domain.

Currently, as an extension of current study, experiments on co-assembly of QDs with CNC is performed in our lab. In this study, ligands engineering on QDs to enable a balanced interaction with CNC in water is desired, with the objective to achieve homogeneous assembly with well-preserved chiral structure across large scale. As for potential unique optical responses, modulation of photoluminescence from QDs is expected in both spectra-shift and polarization.

4.3 Dissemination information

This work has generated one primary paper in preparation, 5 related publications and one conference presentations.

Primary publication:

S. Yu, R. Xiong, S. Kang, K. M. Adstedt, D. Nepal, T. J. Bunning, V. V. Tsukruk, "Integrating Optical Gratings and Lenses into Chiral Biophotonic Materials for Highly Asymmetrical Circular Dichroism", *In preparation*.

Related publications and presentation:

1. R. Xiong, S. Yu, M. J. Smith, J. Zhou, M. Krecker, L. Zhang, D. Nepal, T. J. Bunning, V. V. Tsukruk, "Self-Assembly of Highly Emissive Core/Shell Nanostructures for Chiral Fluorescent Materials", *submitted.*
2. M. J. Smith, C.-H. Lin, S. Yu, V. V. Tsukruk, "Composite Structures with Emissive Quantum Dots for Light Enhancement", *Advanced Optical Materials"*, **2019**, *7*, 1801072.
3. S. Zhang, S. Yu, J. Zhou, J. F. Ponder, M. J. Smith, J. R. Reynolds, V. V. Tsukruk, "Heterogeneous Forward and Backward Scattering Modulation by Polymer-Infused Plasmonic Nanohole Arrays", *J. Mater. Chem. C*, **2019**, *7*, 3090.
4. Y. Chang, Y. J. Yoon, G. Li, E. Xu, S. Yu, C. Lu, Z. Wang, Y. He, C.-H. Lin, B. K. Wagner, V. V. Tsukruk, Z. Kang, N. Thadhani, Y. Jiang, Z. Lin, "All-Inorganic Perovskite Nanocrystals with a Stellar Set of Stabilities and Their Use in White Light-Emitting Diodes", *ACS Appl. Mater. Interfaces*, **2018**, *10*, 37267.
5. C.-H. Lin, Q. Zeng, E. Lafalce, S. Yu, M. J. Smith, Y. J. Yoon, Y. Chang, Y. Jiang, Z. Lin, Z. V. Vardeny, V. V Tsukruk, "Large-Area Lasing and Multicolor Perovskite Quantum Dot Patterns", *Adv. Opt. Mater.*, ***2018***, *6*, 1800474.

6. S. Yu, S. Malak, M. Smith, Y. J. Yoon, C.-H. Lin, J. Jung, Z. Lin, V. V. Tsukruk, “Programmed Emission Transformations—Negative-to-Positive Patterning Using the Decay-to-Recovery Behavior of Quantum Dots”, *MRS Spring Meeting*, **2018**, *Phoenix Arizona*

APPENDIX A. PREPARATION OF CNC SUSPENSION

Wood pulp was obtained from Weyerhaeuser Company. The pulp was first gently washed with tape water to remove impurities and dried at ambient condition for two days. The hydrolysis of the cellulose was done by gradually adding small pieces of dried pulp into 64 wt. % sulfuric acid with constant stirring at 45 °C. The hydrolysis was carried out for 60 minutes and quenched by diluting ten times with DI water. The diluted suspension was kept still for 12 hours, and the supernatant was removed. The extra sulfuric acid was washed from the remaining suspension by two iterations of centrifugation-redispersion. The centrifugation was carried out at 6,000 rpm for 5 minutes, DI water is used to re-disperse the crushed-out cellulose. Dialysis in DI water of the suspension was run for 7 days until the pH value of the water is constant. Dialysis tube with a cut-off at 14kDa was used while the DI water was changed every 12 hours. [90]

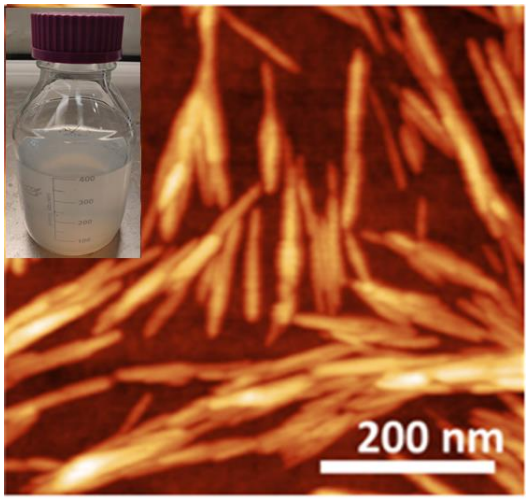

Figure 26 Appearance and dimension of nanocrystals derived from wood pulp.

The suspension after dialysis were then centrifuged at 10,000 rpm for 10 minutes and the crush-outs were removed. The supernatant was then sonicated by tip-sonicator at

500 W for 10 minutes. The resultant concentration of the suspension of CNC is about 0.5-0.7 wt%, and were further concentrated by drying at 40 °C in container until the weight percentage is about 1.5 wt%.

As a result, CNCs prepared from the soft wood pulp by sulfuric acid hydrolysis possesses typical length of 122±52 nm and diameter of 4.9±0.6 nm (Figure 26) and the suspension is clear (Inset) and stable for a long time without any aggregations.

APPENDIX B. CHARACTERIZATION METHODS

B.1 Morphology characterization

Atomic force microscope (AFM) is used to study the surface morphology of patterned CNC films. Icon AFM from Broker was used to investigate the morphology of the film. Cantilever C of XSC 11 from MikroMasch is used in tapping mode. The scan speed ranges from 2 to 20 μm/s, depending on the scanning range. The AFM images were processed using Gwyddion software.

SEM instrument, Hitachi-SU8230, was utilized at 5kV to characterize the microstructure at surface and cross-section of CNC film. Hummer 6 sputter coater was used to deposit 10 nm Au on CNC film.

Contact angle measurement is performed with KSV CAM 101 system, where Sessile droplets of DI water was deposit on the molds and images were captured。

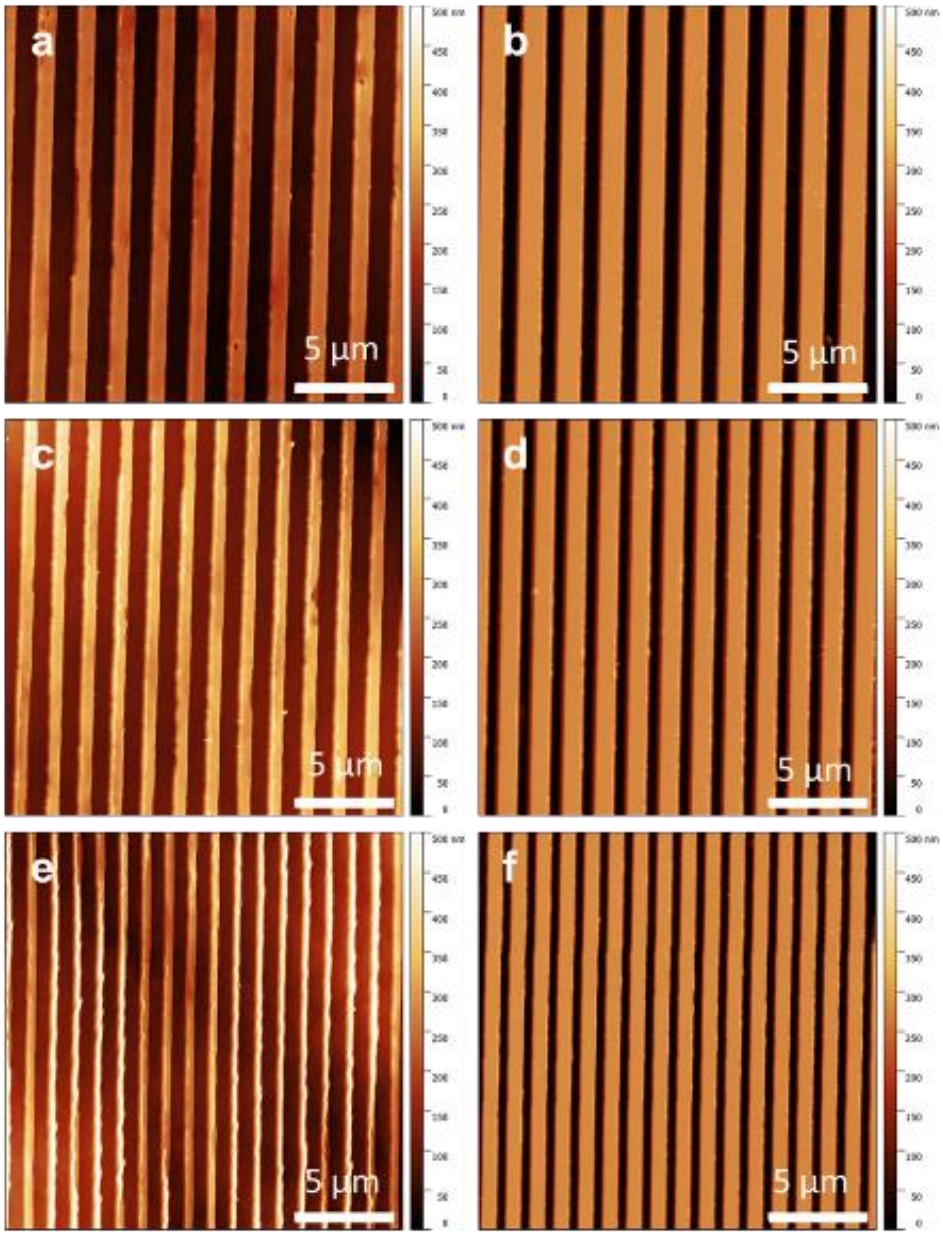

Figure 27 Uniformity of the surface gratings integrated on CNC film.

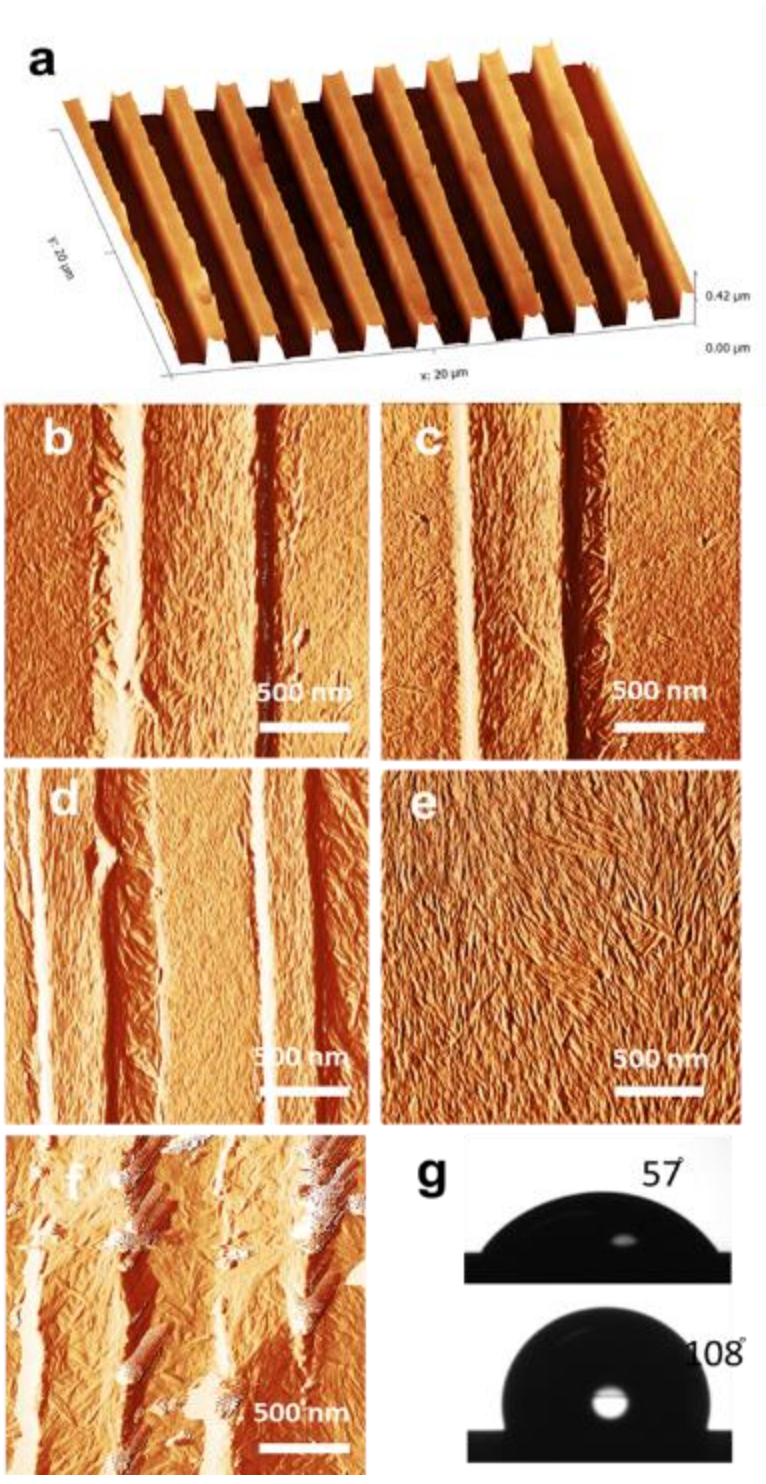

Figure 28 Morphology comparison between CNC films assembled on substrates with different wettability.

B.2 Optical characterization

Several characterization techniques are utilized for the optical properties of the CNC films.

Polarized optical microscope images were collected with Olympus BX51 microscope. White light source from Fiber-Lite DC950 halogen lamp was color-balanced with perfect TiO2 scatter from ThorLabs. The polarizer and analyzer were inserted in the light path with relative angle at 90-degree. Objectives of 10X with numerical aperture NA=0.30, and 50X with NA=0.80 from Olympus were utilized. POM images were taken under both bright-field illumination and dark-field illumination. Stereomicroscope from Omano was used with white light source from Digital Instruments, Inc. FO-50 lamp. Circular polarizer films were obtained from ThorLabs, Inc., to take images in left-handed and right-handed polarized light.

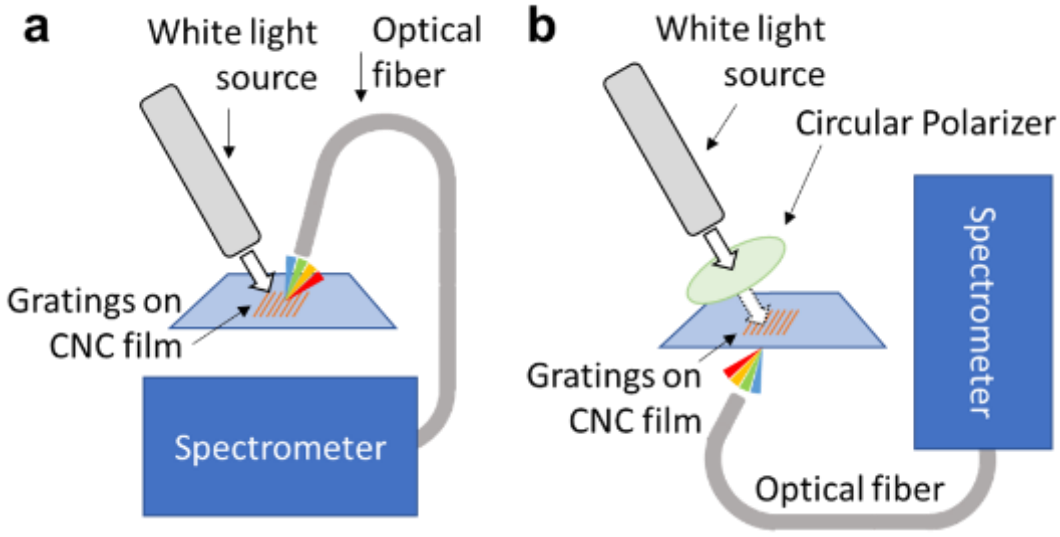

Figure 29 Experiment set-up for reflection and transmittance spectra of CNC film with optical structures.

Circular dichroism spectra were obtained from AP Chirascan™-plus CD Spectrometer from Applied Photophysics Ltd. The CD measurement was done with light beam partially covered by the CNC film to prevent saturating the detector, as reported in literature.[132], [112]

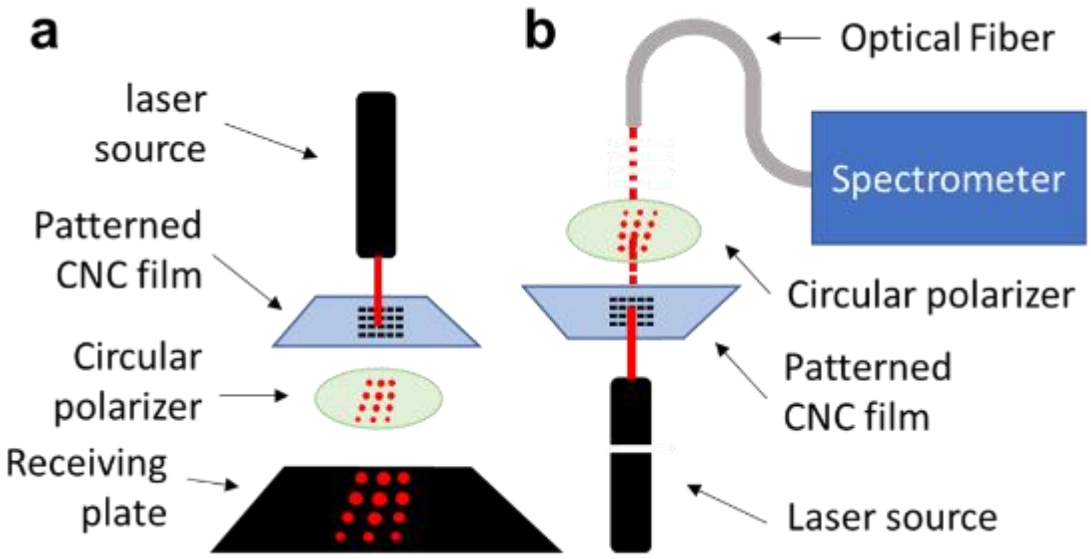

Figure 30 Experiment set-up for laser diffraction and transmittance spectra of CNC film with optical structures.

As for reflectance and transmittance measurement. Avalight-DHS and AvaSpec-2048 from Avantes Inc. were used to collect the reflectance spectra of white light from CNC, while FO-50 from Digital Instruments Inc. was used as a light source for white light transmittance spectra. Red diode laser from PISEN Co Ltd. is used as light source for diffraction pattern generation and laser transmittance spectra measurement. Setup for specific reflection, transmittance measurement and diffraction pattern generation are shown in Figure 29, 30a.

Transmittance of polarizer film from Thorlabs were determined with UV-2450 from Shimadzu Corp., the slit widths of light source and detector were both set at 5 nm for the measurement.

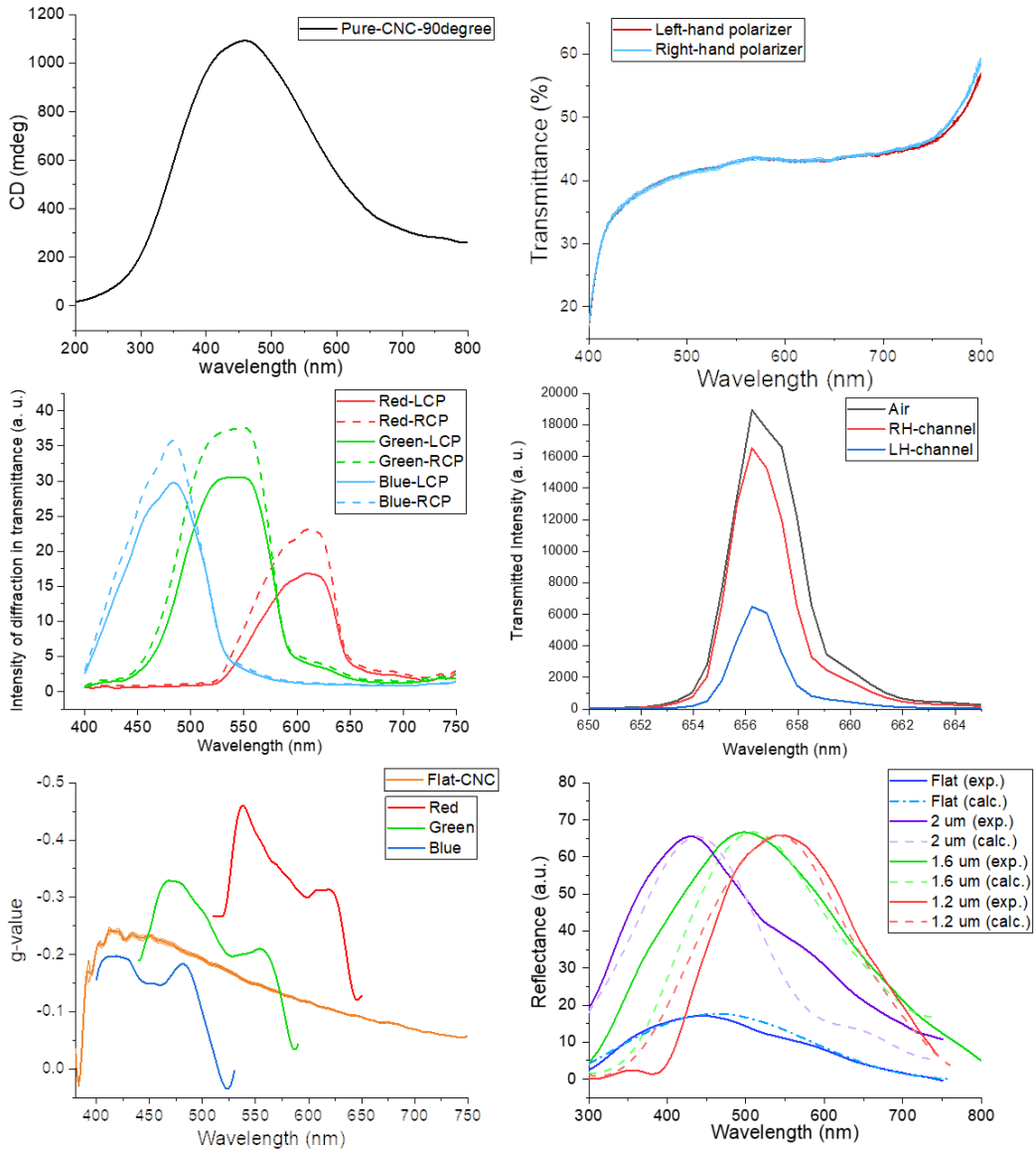

Figure 31 Spectra of CNC films and circular polarizers (transmittance, reflection and circular dichroism).

B.3 Calculation of order parameter

The statistics of orientations of CNC is extracted with imageJ software.[133] The order parameter S is determined with the following equation 12. [134]

$$S = \frac{3\langle cos^2\,\theta\rangle - 1}{2} \tag{12}$$

Where θ is the angle between long axis of CNC and the direction of the confinement trench.

APPENDIX C. COMPARISON OF ASYMMETRIC FACTORS

Table 2 Comparison of asymmetric factors via different CP light generation methods.

Mode	Materials	Asymmetric factor (g)	wavelength	Reference #
Active (fluorescence)	Single enantiomer	-0.00142	543 nm	[135]
	Dye assembled in chiral nanotube	0.0017	581 nm	[125]
	Polymer blend with chiral molecules	0.2-0.5	450 nm	[126]
	Europium and Terbium with chiral ligands	0.1-0.5	N. A.	[127]
	Carbon dots in cellulose nanocrystal	-0.74	424 nm	[113]
Passive (reflection)	Cellulose nanocrystal	-0.87	~ 500 nm	[128]

REFERENCES

[1] S. Johnsen, *The optics of life: a biologist's guide to light in nature*, Princeton University Press, **2012**.
[2] A. R. Parker, *J. Opt. A: Pure Appl. Opt.* **2000**, *2*, R15.
[3] D. Gomez, M. Théry, *Ecology Letters* **2004**, *7*, 279.
[4] A. Sweeney, C. Jiggins, S. Johnsen, *Nature* **2003**, *423*, 31.
[5] H. K. Raut, V. A. Ganesh, A.e S. Nair, S. Ramakrishna, *Energy Environ. Sci.* **2011**, *4*, 3779.
[6] R. L. Rutowski, J. M. Macedonia, J. W. Merry, N. I. Morehouse, K. Yturralde, L. Taylor-Taft, D. Gaalema, D. J. Kemp, R. S. Papke, *Biol. J. Linn. Soc.* **2007**, *90*, 349.
[7] J. Aizenberg, A. Tkachenko, S. Weiner, L. Addadi, G. Hendler, *Nature* **2001**, *412*, 819.
[8] A. R. Parker, H. E. Townley, *Nat. nanotechnol.* **2007**, *2*, 347.
[9] J. M. Benyus, Morrow New York, **1997**.
[10] P. Vukusic, J. R. Sambles, *Nature* **2003**, *424*, 852.
[11] G. England, M. Kolle, P. Kim, M. Khan, P. Muñoz, E. Mazur, J. Aizenberg, *Proc. Natl. Acad. Sci.* **2014**, *111*, 15630.
[12] Y. Liu, J. Shigley, K. Hurwit, *Opt. express* **1999**, *4*, 177.
[13] B. J. Glover, H. M. Whitney, *Ann. Bot.* **2010**, *105*, 505.
[14] S. Vignolini, E. Moyroud, B. J. Glover, U. Steiner, *J. R. Soc., Interface* **2013**, *10*, 20130394.
[15] S. N. Fernandes, Y. Geng, S. Vignolini, B. J. Glover, A. C. Trindade, J. P. Canejo, P. L. Almeida, P. Brogueira, M. H. Godinho, *Macromol. Chem. Phys.* **2013**, *214*, 25.
[16] H. M. Whitney, M. Kolle, P. Andrew, L. Chittka, U. Steiner, B. J. Glover, *Science* **2009**, *323*, 130.
[17] R. L. Antoniou Kourounioti, L. R. Band, J. A. Fozard, A. Hampstead, A. Lovrics, E. Moyroud, S. Vignolini, J. R. King, O. E. Jensen, B. J. Glover, *J. R. Soc., Interface* **2013**, *10*, 20120847.
[18] M. Born, E. Wolf, *Principles of optics: electromagnetic theory of propagation, interference and diffraction of light*, Elsevier, **2013**.
[19] P. Vukusic, J. Sambles, C. Lawrence, R. Wootton, *Proc. R. Soc. Lond. B Biol. Sci.* **1999**, *266*, 1403.
[20] V. Sharma, M. Crne, J. O. Park, M. Srinivasarao, *Mater. Today: Proc.* **2014**, *1*, 161.
[21] V. Sharma, M. Crne, J. O. Park, M. Srinivasarao, *Science* **2009**, *325*, 449.
[22] S. Vignolini, P. J. Rudall, A. V. Rowland, A. Reed, E. Moyroud, R. B. Faden, J. J. Baumberg, B. J. Glover, U. Steiner, *Proc. Natl. Acad. Sci.* **2012**, *109*, 15712.
[23] R. Meister, M.-A. Hallé, H. Dumoulin, P. Pieranski, *Phys. Rev. E* **1996**, *54*, 3771.
[24] J. Chan, *J. Microsc.* **2012**, *247*, 23.
[25] S. N. Fernandes, P. L. Almeida, N. Monge, L. E. Aguirre, D. Reis, C. L. De Oliveira, A. M. Neto, P. Pieranski, M. H. Godinho, *Adv. Mater.* **2017**, *29*, 1603560.
[26] L. Wu, J. He, W. Shang, T. Deng, J. Gu, H. Su, Q. Liu, W. Zhang, D. Zhang, *Adv. Opt. Mater.* **2016**, *4*, 195.

[27] R. Hünig, A. Mertens, M. Stephan, A. Schulz, B. Richter, M. Hetterich, M. Powalla, U. Lemmer, A. Colsmann, G. Gomard, *Adv. Opt. Mater.* **2016**, *4*, 1487.
[28] B. Fritz, R. Hünig, R. Schmager, M. Hetterich, U. Lemmer, G. Gomard, *Bioinspiration Biomimetics* **2017**, *12*, 036011.
[29] J. Aizenberg, G. Hendler, *J. Mater. Chem.* **2004**, *14*, 2066.
[30] K. R. Phillips, G. T. England, S. Sunny, E. Shirman, T. Shirman, N. Vogel, J. Aizenberg, *Chem. Soc. Rev.* **2016**, *45*, 281.
[31] G. M. Nogueira, D. Banerjee, R. E. Cohen, M. F. Rubner, *Langmuir* **2011**, *27*, 7860.
[32] D. P. Puzzo, L. D. Bonifacio, J. Oreopoulos, C. M. Yip, I. Manners, G. A. Ozin, *J. Mater. Chem.* **2009**, *19*, 3500.
[33] P. Kurt, D. Banerjee, R. E. Cohen, M. F. Rubner, *J. Mater. Chem.* **2009**, *19*, 8920.
[34] R. Merindol, S. Diabang, O. Felix, T. Roland, C. Gauthier, G. Decher, *ACS Nano* **2015**, *9*, 1127.
[35] P. Tzeng, D. Hewson, P. Vukusic, S. J. Eichhorn, J. Grunlan, *J. Mater. Chem. C* **2015**, *3*, 4260.
[36] G. von Freymann, V. Kitaev, B. V. Lotsch, G. A. Ozin, *Chem. Soc. Rev.* **2013**, *42*, 2528.
[37] K. E. Shopsowitz, W. Y. Hamad, M. J. MacLachlan, *Angew. Chem. Int. Ed.* **2011**, *50*, 10991.
[38] L. Cademartiri, A. Sutti, G. Calestani, C. Dionigi, P. Nozar, A. Migliori, *Langmuir* **2003**, *19*, 7944.
[39] D. J. Kraft, W. S. Vlug, C. M. van Kats, A. van Blaaderen, A. Imhof, W. K. Kegel, *J. Am. Chem. Soc.* **2008**, *131*, 1182.
[40] K. Busch, S. John, *Phys. Rev. E* **1998**, *58*, 3896.
[41] N. Vogel, L. de Viguerie, U. Jonas, C. K. Weiss, K. Landfester, *Adv. Funct. Mater.* **2011**, *21*, 3064.
[42] A. Stein, F. Li, N. R. Denny, *Chem. Mater.* **2008**, *20*, 649.
[43] D. P. Josephson, M. Miller, A. Stein, *Z. Anorg. Allg. Chem.* **2014**, *640*, 655.
[44] M. J. Smith, C. H. Lin, S. Yu, V. V. Tsukruk, *Adv. Opt. Mater*. **2019**, *7*, 1801072.
[45] R. Menon, A. Patel, D. Gil, H. I. Smith, *Mater. Today* **2005**, *8*, 26.
[46] M. J. Smith, S. T. Malak, J. Jung, Y. J. Yoon, C. H. Lin, S. Kim, K. M. Lee, R. Ma, T. J. White, T. J. Bunning, *ACS Appl. Mater. Interfaces* **2017**, *9*, 17435.
[47] C. H. Lin, Q. Zeng, E. Lafalce, S. Yu, M. J. Smith, Y. J. Yoon, Y. Chang, Y. Jiang, Z. Lin, Z. V. Vardeny, *Adv. Opt. Mater.* **2018**, *6*, 1800474.
[48] Y. Wang, I. Fedin, H. Zhang, D. V. Talapin, *Science* **2017**, *357*, 385.
[49] T. F. Scott, B. A. Kowalski, A. C. Sullivan, C. N. Bowman, R. R. McLeod, *Science* **2009**, *324*, 913.
[50] C. Sun, X. Chen, J. Xu, M. Wei, J. Wang, X. Mi, X. Wang, Y. Wu, Y. Liu, *J. Mater. Chem. A* **2013**, *1*, 4699.
[51] J.-J. Park, P. Prabhakaran, K. K. Jang, Y. Lee, J. Lee, K. Lee, J. Hur, J.-M. Kim, N. Cho, Y. Son, *Nano Lett.* **2010**, *10*, 2310.
[52] R. Krini, C. W. Ha, P. Prabhakaran, H. E. Mard, D. Y. Yang, R. Zentel, K. S. Lee, *Macromol. Rapid Commun.* **2015**, *36*, 1108.
[53] S. Thiele, K. Arzenbacher, T. Gissibl, H. Giessen, A. M. Herkommer, *Sci. Adv.* **2017**, *3*, e1602655.

[54] J. K. Gansel, M. Latzel, A. Frölich, J. Kaschke, M. Thiel, M. Wegener, *Appl. Phys. Lett.* **2012**, *100*, 101109.
[55] C. S. Torres, S. Zankovych, J. Seekamp, A. Kam, C. C. Cedeno, T. Hoffmann, J. Ahopelto, F. Reuther, K. Pfeiffer, G. Bleidiessel, *Mater. Sci. Eng. C* **2003**, *23*, 23.
[56] U. Plachetka, M. Bender, A. Fuchs, B. Vratzov, T. Glinsner, F. Lindner, H. Kurz, *Microelectron. Eng.* **2004**, *73*, 167.
[57] L. J. Guo, *Adv. Mater.* **2007**, *19*, 495.
[58] C. Pina-Hernandez, A. Koshelev, S. Dhuey, S. Sassolini, M. Sainato, S. Cabrini, K. Munechika, *Sci. Rep.* **2017**, *7*, 17645.
[59] T. Mäkelä, M. Kainlauri, P. Willberg-Keyriläinen, T. Tammelin, U. Forsström, *Microelectron. Eng.* **2016**, *163*, 1.
[60] J. J. Amsden, P. Domachuk, A. Gopinath, R. D. White, L. D. Negro, D. L. Kaplan, F. G. Omenetto, *Adv. Mater.* **2010**, *22*, 1746.
[61] A. Espinha, C. Dore, C. Matricardi, M. I. Alonso, A. R. Goñi, A. Mihi, *Nat. Photonics* **2018**, *12*, 343.
[62] K. Gerasopoulos, E. Pomerantseva, M. McCarthy, A. Brown, C. Wang, J. Culver, R. Ghodssi, *Acs Nano* **2012**, *6*, 6422.
[63] A. Dhawan, Y. Du, D. Batchelor, H. N. Wang, D. Leonard, V. Misra, M. Ozturk, M. D. Gerhold, T. Vo-Dinh, *Small* **2011**, *7*, 727.
[64] K. H. Smith, E. Tejeda-Montes, M. Poch, A. Mata, *Chem. Soc. Rev.* **2011**, *40*, 4563.
[65] N. Nuraje, S. Mohammed, L. Yang, H. Matsui, *Angew. Chem. Int. Ed.* **2009**, *48*, 2546.
[66] A. M. Hung, C. M. Micheel, L. D. Bozano, L. W. Osterbur, G. M. Wallraff, J. N. Cha, *Nat. Nanotechnol.* **2010**, *5*, 121.
[67] H. Yi, X. Y. Bao, J. Zhang, C. Bencher, L. W. Chang, X. Chen, R. Tiberio, J. Conway, H. Dai, Y. Chen, *Adv. Mater.* **2012**, *24*, 3107.
[68] M. A. Meitl, Z.-T. Zhu, V. Kumar, K. J. Lee, X. Feng, Y. Y. Huang, I. Adesida, R. G. Nuzzo, J. A. Rogers, *Nat. Mater.* **2006**, *5*, 33.
[69] J. W. Jeong, W. I. Park, L. M. Do, J. H. Park, T. H. Kim, G. Chae, Y. S. Jung, *Adv. Mater.* **2012**, *24*, 3526.
[70] K. Guarini, C. Black, Y. Zhang, H. Kim, E. Sikorski, I. Babich, *J. Vac. Sci. Technol., B: Nanotechnol. Microelectron.: Mater., Process., Meas., Phenom.* **2002**, *20*, 2788.
[71] D. Ye, Q. Cheng, Q. Zhang, Y. Wang, C. Chang, L. Li, H. Peng, L. Zhang, *ACS Appl. Mater. Interfaces* **2017**, *9*, 43154.
[72] P. Tseng, B. Napier, S. Zhao, A. N. Mitropoulos, M. B. Applegate, B. Marelli, D. L. Kaplan, F. G. Omenetto, *Nat. Nanotechnol.* **2017**, *12*, 474.
[73] D. Ye, P. Yang, X. Lei, D. Zhang, L. Li, C. Chang, P. Sun, L. Zhang, *Chem. Mater.* **2018**, *30*, 5175.
[74] H. K. Choi, S. H. Im, O. O. Park, *Langmuir* **2010**, *26*, 12500.
[75] J. H. Moon, S. G. Jang, J. M. Lim, S. M. Yang, *Adv. Mater.* **2005**, *17*, 2559.
[76] W. L. Min, B. Jiang, P. Jiang, *Adv. Mater.* **2008**, *20*, 3914.
[77] Z. Dogic, S. Fraden, *Langmuir* **2000**, *16*, 7820.
[78] E. Grelet, S. Fraden, *Phys. Rev. Lett.* **2003**, *90*, 198302.
[79] X. Mu, D. G. Gray, *Langmuir* **2014**, *30*, 9256–9260.
[80] S. Matsumura, S. Kajiyama, T. Nishimura, T. Kato, *Small* **2015**, *11*, 5127–5133.
[81] G. Nyström, M. Arcari, R. Mezzenga, *Nat. Nanotechnol.* **2018**, *13*, 330.

[82] R. J. Moon, A. Martini, J. Nairn, J. Simonsen, J. Youngblood, *Chem. Soc. Rev.* **2011**, *40*, 3941.
[83] D. Bondeson, A. Mathew, K. Oksman, *Cellulose* **2006**, *13*, 171.
[84] Z. Cheng, H. Ye, F. Cheng, H. Li, Y. Ma, Q. Zhang, A. Natan, A. Mukhopadhyay, Y. Jiao, Y. Li, *Adv. Mater. Interfaces* **2019**, 1802010.
[85] S. Kalia, S. Boufi, A. Celli, S. Kango, *Colloid Polym. Sci.***2014**, *292*, 5.
[86] W. J. Orts, L. Godbout, R. H. Marchessault, J.-F. Revol, *Macromolecules* **1998**, *31*, 5717–5725.
[87] A. Hirai, O. Inui, F. Horii, M. Tsuji, *Langmuir* **2009**, *25*, 497–502.
[88] C. Schütz, M. Agthe, A. B. Fall, K. Gordeyeva, V. Guccini, M. Salajková, T. S. Plivelic, J. P. F. Lagerwall, G. Salazar-Alvarez, L. Bergström, *Langmuir* **2015**, *31*, 6507–6513.
[89] A. Isogai, T. Saito, H. Fukuzumi, *Nanoscale* **2011**, *3*, 71.
[90] S. Beck-Candanedo, M. Roman, D. G. Gray, *Biomacromolecules* **2005**, *6*, 1048.
[91] X. M. Dong, T. Kimura, J.-F. Revol, D. G. Gray, *Langmuir* **1996**, *12*, 2076
[92] X. M. Dong, D. G. Gray, *Langmuir* **1997**, *13*, 2404.
[93] M. Chau, S. E. Sriskandha, D. Pichugin, H. Thérien-Aubin, D. Nykypanchuk, G. Chauve, M. Méthot, J. Bouchard, O. Gang, E. Kumacheva, *Biomacromolecules* **2015**, *16*, 2455.
[94] T. H. Zhao, R. M. Parker, C. A. Williams, K. T. P. Lim, B. Frka-Petesic, S. Vignolini, *Adv. Funct. Mater.* **2018**, *0*, 1804531.
[95] B. Wilts, A. Dumanli, R. Middleton, P. Vukusic, S. Vignolini, *APL Photonics* **2017**, *2*, 040801.
[96] A. G. Dumanli, H. M. van der Kooij, G. Kamita, E. Reisner, J. J. Baumberg, U. Steiner, S. Vignolini, *ACS Appl. Mater. Interfaces* **2014**, *6*, 12302
[97] B. Frka-Petesic, G. Guidetti, G. Kamita, S. Vignolini, *Adv. Mater.* **2017**, *29*, 1701469.
[98] O. O'Keeffe, P.-X. Wang, W. Y. Hamad, M. J. MacLachlan, *J. Phys. Chem. Lett.* **2019**, *10*, 278–282.
[99] B. Wang, A. Walther, *ACS Nano* **2015**, *9*, 10637–10646.
[100] R. Bardet, N. Belgacem, J. Bras, ACS Appl. Mater. Interfaces, 2015, 7, 4010–4018.
[101] K. Yao, Q. Meng, V. Bulone, Q. Zhou, *Adv. Mater.* **2017**, *29*, 1701323.
[102] G. Guidetti, S. Atifi, S. Vignolini, W. Y. Hamad, *Adv. Mater.* **2016**, *28*, 10042.
[103] R. S. Werbowyj, D. G. Gray, Mol. Cryst. *Liq. Cryst.* **1976**, *34*, 97–103.
[104] M. H. Godinho, D. G. Gray, P. Pieranski, *Liq. Cryst.* **2017**, *44*, 2108–2120.
[105] G. Kamita, B. Frka-Petesic, A. Allard, M. Dargaud, K. King, A. G. Dumanli, S. Vignolini, *Adv. Opt. Mater.* **2016**, *4*, 1950.
[106] H.-L. Liang, M. M. Bay, R. Vadrucci, C. H. Barty-King, J. Peng, J. J. Baumberg, M. F. L. D. Volder, S. Vignolini, *Nat. Commun.* **2018**, *9*, 4632.
[107] V. Cherpak, V. F. Korolovych, R. Geryak, T. Turiv, D. Nepal, J. Kelly, T. J. Bunning, O. D. Lavrentovich, W. T. Heller, V. V. Tsukruk, *Nano Lett.* **2018**, *18*, 6770.
[108] R. M. Parker, B. Frka-Petesic, G. Guidetti, G. Kamita, G. Consani, C. Abell, S. Vignolini, *ACS Nano* **2016**, *10*, 8443.
[109] X. Mu, D. G. Gray, *Cellulose* **2015**, *22*, 1103.
[110] S. N. Fernandes, P. L. Almeida, N. Monge, L. E. Aguirre, D. Reis, C. L. P. de Oliveira, A. M. F. Neto, P. Pieranski, M. H. Godinho, *Adv. Mater.* **2017**, *29*, 1603560.
[111] Y. Cao, W. Y. Hamad, M. J. MacLachlan, *Adv. Opt. Mater.* **2018**, *6*, 1800412.

[112] T. D. Nguyen, W. Y. Hamad, M. J. MacLachlan, *Adv. Funct. Mater.* **2014**, *24*, 777.
[113] H. Zheng, B. Ju, X. Wang, W. Wang, M. Li, Z. Tang, S. X.-A. Zhang, Y. Xu, *Adv. Opt. Mater.* **2018**, *6*, 1801246.
[114] O. Kose, A. Tran, L. Lewis, W. Y. Hamad, M. J. MacLachlan, *Nat. Commun.* **2019**, *10*, 510.
[115] T. K. Gaylord, M. Moharam, *Proc. of the IEEE* **1985**, *73*, 894.
[116] W. S. John, W. Fritz, Z. Lu, D.-K. Yang, *Phys. Rev. E* **1995**, *51*, 1191.
[117] J. P. Lagerwall, C. Schütz, M. Salajkova, J. Noh, J. H. Park, G. Scalia, L. Bergström, *NPG Asia Mater.* **2014**, *6*, e80.
[118] D. Levine, P. J. Steinhardt, *Phys. Rev. Lett.* **1984**, *53*, 2477.
[119] Z. V. Vardeny, A. Nahata, A. Agrawal, *Nat. Photonics* **2013**, *7*, 177.
[120] J. A. Currivan, S. Siddiqui, S. Ahn, L. Tryputen, G. S. Beach, M. A. Baldo, C. A. Ross, *J. Vac. Sci. Technol., B: Nanotechnol. Microelectron.: Mater., Process., Meas., Phenom.* **2014**, *32*, 021601.
[121] J. Brzoska, I. B. Azouz, F. Rondelez, *Langmuir* **1994**, *10*, 4367.
[122] K. O. Hill, B. Malo, F. Bilodeau, D. Johnson, J. Albert, *App. Phys. Lett.* **1993**, *62*, 1035.
[123] V. Guccini, S. Yu, M. Agthe, K. Gordeyeva, Y. Trushkina, A. Fall, C. Schütz, G. Salazar-Alvarez, *Nanoscale* **2018**, *10*, 23157.
[124] R. A. Chowdhury, S. X. Peng, J. Youngblood, *Cellulose* **2017**, *24*, 1957.
[125] J. Han, J. You, X. Li, P. Duan, M. Liu, *Adv. Mater.* **2017**, *29*, 1606503.
[126] A. P. C. Almeida, J. P. Canejo, S. N. Fernandes, C. Echeverria, P. L. Almeida, M. H. Godinho, *Adv. Mater.* **2013**, *30*, 1703655.
[127] R. Carr, N. H. Evans, D. Parker, *Chem. Soc. Rev.* **2012**, *41*, 7673.
[128] H. Zheng, W. Li, W. Li, X. Wang, Z. Tang, S. X.-A. Zhang, Y. Xu, *Adv. Mater.* **2018**, *30*, 1705948.
[129] P.-X. Wang, W. Y. Hamad, M. J. MacLachlan, *Nat. Commun.* **2016**, *7*, 11515.
[130] F. Zinna, U. Giovanella, L. D. Bari, *Adv. Mater.* **2015**, *27*, 1791.
[131] T. Gissibl, S. Thiele, A. Herkommer, H. Giessen, *Nat. Photonics* **2016**, *10*, 554.
[132] D. Qu, H. Zheng, H. Jiang, Y. Xu, Z. Tang, *Adv. Opt. Mater.* **2019**, 1801395.
[133] A. Boudaoud, A. Burian, D. Borowska-Wykręt, M. Uyttewaal, R. Wrzalik, D. Kwiatkowska, O. Hamant, *Nat. Protoc.* **2014**, *9*, 457.
[134] R. A. Chowdhury, S. X. Peng, J. Youngblood, *Cellulose* **2017**, *24*, 1957.
[135] Y. Tang, A. E. Cohen, *Science* **2011**, *332*, 333.